

Article

Effect of Pre-Injection on Combustion and Emission Characteristics of a Diesel Engine Fueled with Diesel/Methanol/*n*-Butanol Blended Fuel

Zhiqiang Wang ^{1,2} and Lijun Li ^{1,*}

¹ School of Mechanical and Electrical Engineering, Central South University of Forestry and Technology, Changsha 410004, China; zqwang@hnust.edu.cn

² School of Informational and Electrical Engineering, Hunan University of Science and Technology, Xiangtan 411201, China

* Correspondence: T19930431@csuft.edu.cn

Abstract: In this study, the combustion and emission characteristics of a diesel/methanol/*n*-butanol blended fuel engine with different pre-injection timings and pre-injection mass ratios were investigated by a computational fluid dynamics (CFD) model. The CFD model was verified by the measured results and coupled with a simplified chemical kinetics mechanism. Firstly, the corresponding three-dimensional CFD model was established by CONVERGE software and the CHEKMIN program, and a chemical kinetic mechanism containing 359 reactions and 77 species was developed. Secondly, the combustion and emission characteristics of the diesel engine with different diesel/methanol/*n*-butanol blended fuels were analyzed and discussed. The results showed that increases in the pre-injection timing and the pre-injection mass ratio could increase cylinder pressure and cylinder temperature and decrease soot, HC, and CO emissions. At 100% load, the maximum cylinder pressures at the start of pre-injection timing from -15°CA to -45°CA , were 7.71, 9.46, 9.85, 9.912, and 9.95 MPa, respectively. The maximum cylinder pressures at pre-injection fuel mass ratios from 0.1 to 0.9 were 7.98, 9.10, 9.96, 10.52, and 11.16 MPa, respectively. At 50% load, with increases of the pre-injection timing and pre-injection fuel mass ratio, the soot emission decreased by 7.30%, 9.45%, 27.70%, 66.80%, 81.80% and 11.30%, 20.03%, 71.32%, 83.80%, 93.76%, respectively, and CO emissions were reduced by 5.77%, 12.31%, 22.73%, 53.59%, 63.22% and 8.29%, 43.97%, 53.59%, 58.86%, 61.18%, respectively. However, with increases of the pre-injection timing and pre-injection mass ratio, NO_x emission increased. In addition, it was found that the optimal pre-injection timing and optimal pre-injection mass ratio should be -30°CA and 0.5, respectively. Therefore, through this study we can better understand the potential interaction of relevant parameters and propose pre-injection solutions to improve combustion and emission characteristics.



Citation: Wang, Z.; Li, L. Effect of Pre-Injection on Combustion and Emission Characteristics of a Diesel Engine Fueled with Diesel/Methanol/*n*-Butanol Blended Fuel. *Processes* **2022**, *10*, 60. <https://doi.org/10.3390/pr10010060>

Academic Editor:
Alessandro D'Adamo

Received: 27 November 2021

Accepted: 24 December 2021

Published: 28 December 2021

Publisher's Note: MDPI stays neutral with regard to jurisdictional claims in published maps and institutional affiliations.



Copyright: © 2021 by the authors. Licensee MDPI, Basel, Switzerland. This article is an open access article distributed under the terms and conditions of the Creative Commons Attribution (CC BY) license (<https://creativecommons.org/licenses/by/4.0/>).

Keywords: diesel/methanol/*n*-butanol blended fuel; pre-injection; diesel engine; combustion and emission characteristics

1. Introduction

Due to its high thermal efficiency, good reliability, and sufficient and stable power, the diesel engine has been favored for a long time by the fields of national defense and the military, and in power plants, transportation, engineering machinery, and agricultural machinery [1]. It has made great contributions to improvements in social development and at the economic level [2]. However, the development of the diesel engine has faced great challenges with the collection and utilization of oil resources [3]. This is mainly reflected in energy shortages caused by the massive utilization of fossil fuels and the environmental pollution caused by combustion emissions [4]. Therefore, facing the global energy crisis and environmental degradation [5], how to find renewable energy, and how to effectively reduce diesel engine emissions are the problems that need to be solved in today's

society [6]. An important method is to use alternative fuels in diesel engines [7]. The use of alternative fuels in diesel engines is considered to be an effective measure to reduce their dependence on diesel and reduce pollutant emissions [8]. Therefore, the engine parameters of various biofuels (such as biodiesel and alcohol) need to be optimized to enhance their characteristics [9]. As a result, research on exploring new renewable alternative fuels has attracted more and more attention [10,11].

Methanol and ethanol belong to low-carbon chain alcohols. As pure diesel additives, their oxygen-containing structural characteristics can improve the engine's combustion process and reduce soot emission [12]. Compared with traditional fossil fuels, methanol has obvious advantages [13]. For example, with a high octane number and good seismic performance, the engine compression ratio can be appropriately increased to improve engine performance and reduce fuel consumption. Moreover, methanol has a large latent heat of vaporization and lower combustion temperature in the cylinder, which can reduce heat loss and NO_x emission [14]. Park et al. [15] studied the effect of methanol addition on the performance and emission characteristics of diesel engines. The results showed that the cylinder pressure, cylinder temperature, and NO_x emission decreased with increased methanol content. However, due to the characteristics of a low cetane number and high latent heat of evaporation of methanol, spontaneous combustion occurs easily [16]. In addition, due to the low calorific value, poor stability and immiscibility with diesel [17], the application of methanol in diesel engines is greatly hindered [18,19].

Compared with other fuels, *n*-butanol has a low latent heat of vaporization and ignition temperature. Thus, the cold start characteristic of the diesel engine can be greatly improved [20]. In addition, *n*-butanol is more resistant to water pollution and less corrosive. The most important point is that *n*-butanol is more miscible with diesel [21]. Moreover, the viscosity and density of *n*-butanol are similar to diesel [22]. Lots of experts have carried out research on *n*-butanol. For example, Satsangi et al. [23] studied the combustion and emission characteristic of a diesel engine fueled with four different diesel/*n*-butanol blends. The results showed that compared with pure diesel, the maximum cylinder pressure of diesel engine fuel with diesel/*n*-butanol blends increased by 5.3% and the emission characteristics of blends of diesel engine fuel with diesel/*n*-butanol also improved. Rakopolulos et al. [24] studied the effect of diesel/*n*-butanol blends on the performance and emission characteristics of a diesel engine. The results showed that the brake specific fuel consumption (BSFC) of a diesel engine fueled with a diesel/*n*-butanol blend increased due to lower calorific values than pure diesel. However, the brake thermal efficiency (BTE) improved due to the improved combustion caused by the *n*-butanol content in the diesel/*n*-butanol blend.

To improve engine performance, combustion and emission, this problem can be overcome by changing factors, such as the pilot fuel volume, injection timing, gaseous fuel composition and intake conditions [25]. Pre-injection is a form of multi-injection and means that a small amount of fuel is injected first, before the main injection. The main parameters, such as the pre-injection timing, pre-injection fuel mass ratio, and injection duration, will significantly affect combustion and emission characteristics [26]. In diesel engines, many researchers had studied the effects of pre-injection on engine combustion and emission characteristics. For example, Lu et al. [27] and Wang et al. [28] investigated the effects of the main injection mode, injection ratio, and injection timing on the combustion and emission characteristics of a high-load, low-speed diesel engine. The results showed that the advanced pre-injection timing and increased pre-injection fuel mass ratio could reduce knock and NO_x emission. Similarly, Liu et al. [29] studied the effects of injection timing on the performance and exhaust emissions of the engine diesel/methanol compound combustion (DMCC) mode. The results showed that under the DMCC model, the peak cylinder pressure and maximum heat release rate in the cylinder were increased, and the intake air temperature, NO_x, and soot emissions were reduced. Liu et al. [30] investigated the effects of each parameter on the emission characteristics of a diesel engine fueled with an *n*-butanol/diesel blended fuel under two combustion strategies, early injection partial premixed combustion (PPC) and pre-injection PPC. The results showed that the

premixed combustion ratio and the average diameter of particulate matter decreased with an increasing pre-injection ratio. Bhowmick et al. [31] investigated the effect of different injection strategies on a common rail direct injection engine. The results showed that the 10% pilot fuel and 90% main injection strategy (B10@P10-M90) outperformed the pure diesel fuel among all the injection strategies. Compared to all the injection strategies, the B10@P10-M90 had the highest efficiency of 35.8% and the lowest fuel consumption of 0.25 kg/(kW·h). The carbon monoxide (CO) and hydrocarbon (HC) emissions were lower than all the tested emissions of all the samples tested.

With the development of computer science and information technology, the combustion chemical kinetic mechanism has been further expanded and examined in depth. Moreover, in the manufacturing industry, design, experimentation, and prototyping are very difficult and expensive [32]. Thus, the simulation method has been applied in the internal combustion engine field [33]. Simulations can not only greatly save in the cost, but also greatly shorten the research cycle [34]. The numerical simulation has been widely accepted as a good way to study diesel engines. This is because the three-dimensional computational fluid dynamics (CFD) simulation method combined with the chemical kinetic mechanism can accurately predict the combustion process [35]. Many researchers had studied *n*-butanol/diesel blends by the CFD simulation method. Gong et al. [36] used AVL-Fire to simulate the effects of injection and ignition timing on engine combustion and the in-cylinder formaldehyde and unburned methanol emissions during the cold start of a methanol engine. Zang et al. [37] used an improved KIVA-3 V code coupled with the CHEMKIN solver to simulate the combustion and emission of a diesel/methanol dual fuel (DMDF) engine. They found that the CFD method could be considered as an effective method and could accurately predict the cylinder combustion process.

In conclusion, a large number of researchers have used CFD software to study the effects of diesel/methanol and diesel/*n*-butanol blended fuels on engine combustion and emission characteristics, and have further optimized engine combustion and emission combined, using a pre-injection strategy. However, very few have used CONVERGE Studio software to simulate engine combustion chambers with diesel/methanol/*n*-butanol blends to investigate the effects of pre-injection timing and the pre-injection fuel mass ratio on engine combustion and emission characteristics.

As mentioned above, the behaviors of diesel/methanol/*n*-butanol blended fuels are different due to the different thermos-physical properties. In this paper, CONVERGE software combined with the Chemkin code was employed to simulate the cylinder combustion process. Firstly, according a four-stroke diesel engine, the CFD model was developed and then validated by the experimental results at different loads. Then, the combustion processes of diesel/methanol/*n*-butanol blends were simulated and compared. Finally, the effects of the pre-injection timing and pre-injection mass ratio on the combustion and emission characteristics of a diesel engine fueled with diesel/methanol/*n*-butanol blends were studied. Therefore, this study helps to optimize the combustion and emission characteristics of diesel/methanol/*n*-butanol blends for diesel engines, reducing the dependence on petroleum fuels, improving diesel engine performance, and reducing diesel engine pollutant emissions.

2. Materials and Methods

In this study, the numerical simulations were performed by using CONVERGE software combined with a detailed chemical kinetic mechanism. A series of numerical sub-models were used to simulate the combustion process and pollutant formation mechanism of the diesel/methanol/*n*-butanol (DMB) blended fuel engine.

2.1. Turbulence Model

The RNG k - ϵ turbulence model was used for the calculations because this turbulence model fully considers the change of gas density in the wall boundary layer [38] and the influence of the vortex on turbulence and improves the accuracy of vortex flow [39].

Moreover, the model has low requirements for the grid quality near the wall. The principle is to introduce turbulent kinetic energy k and a turbulent dissipation rate ε based on the Navier-Stokes equation by using the basic idea of RNG. The expression is as follows [40]:

$$\frac{\partial(\rho k_t)}{\partial t} + \text{div}(\rho k_t U) = \text{div}[\alpha_k \mu_{eff} \text{grad } k_t] + \tau_{ij} \cdot S_{ij} - \rho \varepsilon \quad (1)$$

$$\frac{\partial(\rho \varepsilon)}{\partial t} + \text{div}(\rho \varepsilon U) = \text{div}[a_\varepsilon \mu_{eff} \text{grad } \varepsilon] + C_{1\varepsilon}^* \frac{\varepsilon}{k_t} - \tau_{ij} \cdot S_{ij} - C_{2\varepsilon} \rho \frac{\varepsilon^2}{k_t} \quad (2)$$

with,

$$\tau_{ij} = -\rho \overline{u'_i u'_j} = 2\mu_t S_{ij} - \frac{2}{3}\rho k_t \delta_{ij} \quad (3)$$

and

$$\mu_{eff} = \mu + \mu_t \quad \mu_t = \rho C_\mu \frac{k_t^2}{\varepsilon} \quad (4)$$

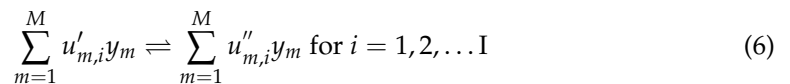
$$C_{1\varepsilon}^* = C_{1\varepsilon} - \frac{\eta(1 - \frac{\eta}{\eta_0})}{1 + \beta\eta^3} \quad \eta = \frac{k_t}{\varepsilon} \sqrt{2S_{ij} \cdot S_{ij}} \quad (5)$$

where ρ is the density, g/cm^3 ; k_t is the turbulent kinetic energy, m^2/s^2 ; U is the fluid velocity, m/s ; S_{ij} is the turbulent source term; ε is the turbulent dissipation rate; μ is the molecular viscosity, $\text{Pa}\cdot\text{s}$. The Kronecker delta δ_{ij} is given by $\delta_{ij} = 1$ if $i = j$ and $\delta_{ij} = 0$ if $i \neq j$. $C_{1\varepsilon} = 1.42$, $C_{2\varepsilon} = 1.68$, $\alpha_k = \alpha_\varepsilon = 1.39$, $C_\mu = 0.0845$, $\eta_0 = 4.377$, and $\beta = 0.012$.

2.2. Combustion Model

In addition, the SAGE model was chosen in this study to simulate the combustion process of a DMB blended fuel engine with a chemical kinetic mechanism including 77 species and 359 reactions.

According to the description of Turns [41], a multistep chemical reaction mechanism can be written as follows:



where $u'_{m,i}$ is the stoichiometric coefficients for the reactants for species m and reaction i ; $u''_{m,i}$ is the stoichiometric coefficients for the products for species m and reaction i ; I is the total number of reactions; and y_m is the chemical symbol for the species m . The net productivity of species m is

$$\dot{\omega}_m = \sum_{i=1}^I u_{m,i} q_i \quad \text{for } m = 1, 2, \dots, M \quad (7)$$

where M is the total number of species and

$$u_{m,i} = u''_{m,i} - u'_{m,i} \quad (8)$$

The reaction rate parameter q_i of the i^{th} reaction is

$$q_i = k_{i,f} \prod_{m=1}^M [X_m]^{u'_{m,i}} - k_{i,r} \prod_{m=1}^M [X_m]^{u''_{m,i}} \quad (9)$$

where X_m is the molar concentration of species m , mol/L ; $k_{i,f}$ and $k_{i,r}$ are the forward and reverse rate coefficients for reaction i . In SAGE, the forward rate coefficient is expressed in Arrhenius form as

$$k_{i,f} = A_i T^{\beta_i} \exp\left(\frac{-E_i}{RT}\right) \quad (10)$$

where A_i is the pre-exponential factor; β_i is the temperature exponent; E_i is the activation energy, cal/mol; R is the ideal gas constant; and T is the temperature, K. In addition, the reverse rate coefficient can either be specified in an analogous fashion as in Equation (11), or calculated from the equilibrium coefficient $K_{i,c}$ as

$$K_{i,c} = \frac{k_{i,f}}{k_{i,r}} \quad (11)$$

The equilibrium coefficient $K_{i,c}$ is determined by thermodynamic properties

$$K_{i,c} = K_{i,p} \left(\frac{P_{atm}}{RT} \right)^{\sum_{m=1}^M u_{m,i}} \quad (12)$$

where P_{atm} is the atmospheric pressure, Pa. The equilibrium constant $K_{i,p}$ is obtained via

$$K_{i,p} = \exp \left(\frac{\Delta S_i^1}{R} - \frac{\Delta H_i^1}{RT} \right) \quad (13)$$

The Δ refers to the change that occurs in passing completely from reactants to products in the i^{th} reaction, specifically,

$$\frac{\Delta S_i^1}{R} = \sum_{m=1}^M u_{m,i} \frac{S_m^1}{R} \quad (14)$$

$$\frac{\Delta H_i^1}{RT} = \sum_{m=1}^M u_{m,i} \frac{H_m^1}{RT} \quad (15)$$

where S denotes entropy, J/(mol·K); and H denotes enthalpy, kJ/mol.

2.3. Spray Model

Based on the physical characteristics of the fuel spray and blending process, the Kelvin-Helmholtz and Rayleigh-Taylor (KH-RT) model is employed to simulate the spray breakup process of fuel. In this model, the KH mechanism and the RT mechanism were used to simulate the primary and secondary crushing, respectively [42].

The following formula can express the radius change rate of droplets in the KH model:

$$r = B_o \Lambda_{KH} \quad (16)$$

$$v_n = C_1 \Lambda_{KH} \Omega_{KH} \quad (17)$$

$$\tau_{KH} = \frac{3.726 B_b r_i}{\Lambda_{KH} \Omega_{KH}} \quad (18)$$

where r is the droplet size, mm; B_o is the model size constant; Λ_{KH} is the wavelength of the fastest growing wave on the surface of the initial liquid column, mm; v_n is the model velocity constant; C_1 is the model constant; Ω_{KH} is the wave growth rate of the fastest growing wave on the surface of the initial liquid column, mm/s; τ_{KH} is the breakup time, s; B_b is the model breakup time constant; and r_i is the initial droplet radius, mm.

The RT model obtains the wavelength (Λ_{RT}) and the wave growth rate (Ω_{RT}) by solving the discrete equation:

$$\Omega_{RT} = \left(\frac{2}{3\sqrt{3}\sigma_s} \frac{[-g_t(\rho_l - \rho_g)]^{3/2}}{\rho_l + \rho_g} \right)^{1/2} \quad (19)$$

where g_t is the acceleration in the direction of motion, m/s²; ρ_l is the density of the liquid phase, g/cm³; ρ_g is the density of the gas phase, g/cm³; and σ_s is the surface tension coefficient.

The wavelength and wave number (K_{RT}) are:

$$\Lambda_{RT} = \frac{2\pi C_{RT}}{K_{RT}} \quad (20)$$

$$K_{RT} = \left(\frac{-g_t(\rho_l - \rho_g)}{3\sigma_s} \right) \quad (21)$$

where C_{RT} is a parameter that can be adjusted through the measurement results related to the nozzle conditions. In this paper, it is taken as 0.1.

The droplet breaking time scale and new droplet radius (r_{new}) are:

$$\tau_{RT} = \frac{C_\tau}{\Omega_{RT}} \quad (22)$$

$$r_{new} = \frac{\pi C_{RT}}{K_{RT}} \quad (23)$$

where C_τ is the model breakup time constant.

The RT breakup length (L_b) equation is given by [43]:

$$L_b = C_{bl} \sqrt{\frac{\rho_l}{\rho_g}} d_o \quad (24)$$

where C_{bl} is the RT model breakup length constant; and d_o is the nozzle diameter, mm.

Due to the low energy substitution rate and less collision with the wall, the rebound/slide model [43] was more suitable for the interaction between droplets and solid surfaces. The model includes two impact regimes, rebound and slide, which are based on the Weber number We_i of the incoming drop at impact.

$$We_i = \frac{\rho_f V_n^2 d_o}{\sigma_f} \quad (25)$$

where ρ_f is the fluid density (kg/m^3); V_n is the velocity component normal to the surface, m/s ; d_o is the characteristic length, m ; σ_f is the surface tension coefficient of the fluid, N/m .

If We_i is less than 80 (rebound regime), the drop rebounds elastically with a normal velocity given by [43] as

$$V_{n,o} = V_{n,i} \sqrt{\frac{We_o}{We_i}} \quad (26)$$

where $V_{n,o}$ is the velocity component normal to the surface of the outgoing drop, m/s ; $V_{n,i}$ is the velocity component normal to the surface of the incoming drop, m/s . The Weber number of the outgoing drop We_o is obtained from:

$$We_o = 0.678 We_i \exp(-0.04415 We_i) \quad (27)$$

If We_i is greater than 80, the jet model of Naber and Reitz [44] is used to update the drop velocity.

Moreover, the Frossling model [45] was used to predict droplet evaporation. The Frossling correlation is

$$\frac{dr_i}{dt} = -\frac{\alpha_{spray} \rho_g D}{2\rho_l r_i} B_d Sh_d \quad (28)$$

where α_{spray} is the scaling factor for the mass transfer coefficient; D is the mass diffusivity of liquid vapor in air, m^2/s . It defines B_d as:

$$B_d = \frac{Y_1^* - Y_1}{1 - Y_1^*} \quad (29)$$

where Y_1^* is the vapor mass fraction at the drop's surface, %; Y_1 is the vapor mass fraction, %; and Sh_d is the Sherwood number given by:

$$Sh_d = \left(2.0 + 0.6Re_d^{1/2}Sc^{1/3}\right) \frac{\ln(1 + B_d)}{B_d} \quad (30)$$

where

$$Re_d = \frac{\rho_g |u_i + u_i' - v_i| d}{\mu_{air}} \quad (31)$$

where u_i and u_i' are the local mean and turbulent fluctuating gas velocities, respectively, m/s; v_i is the velocity of the droplet, m/s; d is the drop diameter, mm; and μ_{air} is the air viscosity which is evaluated at the temperature \hat{T} given by [45]

$$\hat{T} = \frac{T_{gas} + 2T_d}{3} \quad (32)$$

where T_{gas} is the gas temperature, K; and T_d is the drop temperature, K.

Furthermore, the Sc is the Schmidt number of air given by

$$Sc = \frac{\mu_{air}}{\rho_{gas} D} \quad (33)$$

In addition the mass diffusivity of liquid vapor in air D is determined from the correlation:

$$\rho_g D = 1.293 D_0 (\hat{T}/273)^{n_0 - 1} \quad (34)$$

where D_0 and n_0 are model constants.

$$Y_1^* = \frac{MW_{C_nH_{2m}}}{MW_{C_nH_{2m}} + MW_{mix} \left(\frac{p_{gas}}{p_v} - 1\right)} \quad (35)$$

where $MW_{C_nH_{2m}}$ is the molecular weight of the C_nH_{2m} , Da; MW_{mix} is the molecular weight of the mixture (not including vapor from the liquid species), Da; p_{gas} is the gas pressure, Pa; and p_v is the vapor pressure at the current droplet temperature, Pa.

2.4. Emission Model

The formation of NO_x was modeled using the Extended Zeldovich mechanism proposed by Heywood [46]. This model can better predict the formation of NO. The expression is as follows:



The rate constants for the reactions in Equations (36)–(38) are

$$k_{1,f} = 7.6 \times 10^{13} \exp\left(\frac{-38000}{T}\right) \quad (39)$$

$$k_{1,r} = 1.6 \times 10^{13} \quad (40)$$

$$k_{2,f} = 6.4 \times 10^9 T \exp\left(\frac{-3150}{T}\right) \quad (41)$$

$$k_{2,r} = 1.5 \times 10^9 T \exp\left(\frac{-19500}{T}\right) \quad (42)$$

$$k_{3,f} = 4.1 \times 10^{13} \quad (43)$$

$$k_{3,f} = 2.0 \times 10^{14} \exp\left(\frac{-23650}{T}\right) \quad (44)$$

where k is the rate constant, $\text{cm}^3/(\text{mol}\cdot\text{s})$; the subscript f denotes a forward reaction, and the subscript r denotes a reverse reaction.

The Hiroyasu-NSC soot model was used to predict soot emission [47]. The expression is as follows:

$$\frac{dm_s}{dt} = \frac{dm_{sf}}{dt} - \frac{dm_{so}}{dt} \quad (45)$$

$$\frac{dm_{sf}}{dt} = A_f m_f P^{0.5} \exp\left(\frac{-E_{sf}}{RT}\right) \quad (46)$$

$$\frac{dm_{so}}{dt} = A_o m_s \frac{P_{O_2}}{P} P^{1.8} \exp\left(\frac{-E_{so}}{R_u T}\right) \quad (47)$$

where m_s is the total amount of soot, kg; m_{sf} is the amount of soot generation, kg; m_{so} is the amount of soot oxidation, kg; A_f is the constant; m_f is the fuel evaporation, kg; P is the cylinder pressure, Pa; E_{sf} represents the activation energy in the process of formation; A_o is the constant; P_{O_2} is the partial pressure of oxygen, Pa; E_{so} represents the activation energy in the process of oxidation, kJ; and R_u is the gas constant, $\text{cal}/(\text{K}\cdot\text{g}\cdot\text{mol})$.

2.5. Boundary Condition

In this paper, a four-cylinder, four-stroke diesel engine was used for experiments. The fuel injection quantity was obtained and adjusted by the electronic control unit of the diesel engine. The diesel engine specifications and boundary conditions are shown in Table 1. In addition, the friction work of the diesel engine was obtained by an empirical equation. The boundary conditions were obtained by the experiment. However, the boundary conditions which were not measured by the experiment were calculated by the validated AVL-BOOST model.

Table 1. Engine specifications and boundary conditions.

Type	Value	Type	Value
Bore \times stroke (mm)	190 \times 210	Compression ratio	14
Number of cylinders	4	Head temperature (K)	553
Engine speed (rpm)	2000	Piston temperature (K)	423
Effective power (kW)	220	Wall temperature (K)	433
Nozzle radius (mm)	0.26	Temperature at IVC (K)	341
Fuel injection holes	8	Pressure at IVC (bar)	1.97
Cylinder diameter (mm)	190	Turbulent kinetic energy (m^2/s^2)	62.0271
Connecting rod (mm)	410	Turbulent dissipation (m^2/s^3)	17183.4

2.6. Computational Mesh

In this study, the engine's combustion chamber was modeled and calculated by using CONVERGE software to simulate the combustion process of a DMB blended fuel engine. Since the fuel injection nozzle was located on the central axis of the cylinder block close to the cylinder head, the eight fuel injection nozzle holes were symmetrically distributed. In order to reduce the calculation time, the cylinder block model was simplified to a 45° sector of a single fuel nozzle hole. The geometry of the eighth combustor is shown in Figure 1. All the meshes have fine mesh near the piston crevice, fuel spray path and injector nozzle regions.

In addition, the calculation time and accuracy of the CFD model are determined by the grid size [48]. Figure 2 shows the cylinder pressure generated by the grids of the DMB blended fuel at 100% load. The results showed that there was no significant difference between 1.2 mm and 1.4 mm grids. Therefore, due to a higher accuracy and lower calculation time, the best 1.4 mm grid was used to simulate the combustion process [49].

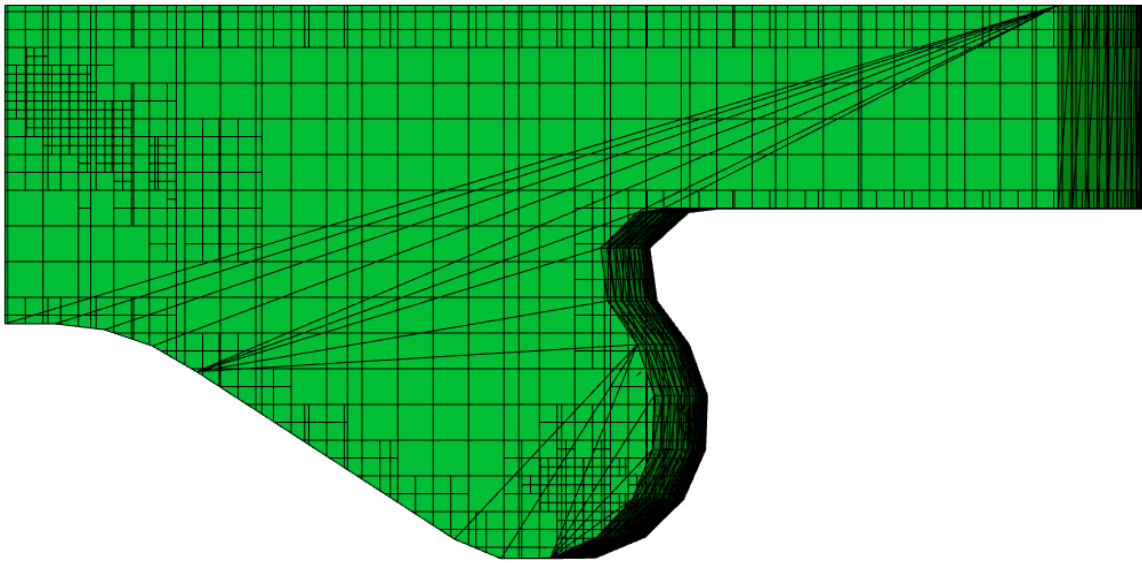


Figure 1. The geometric model of the combustion chamber in the CONVERGE environment.

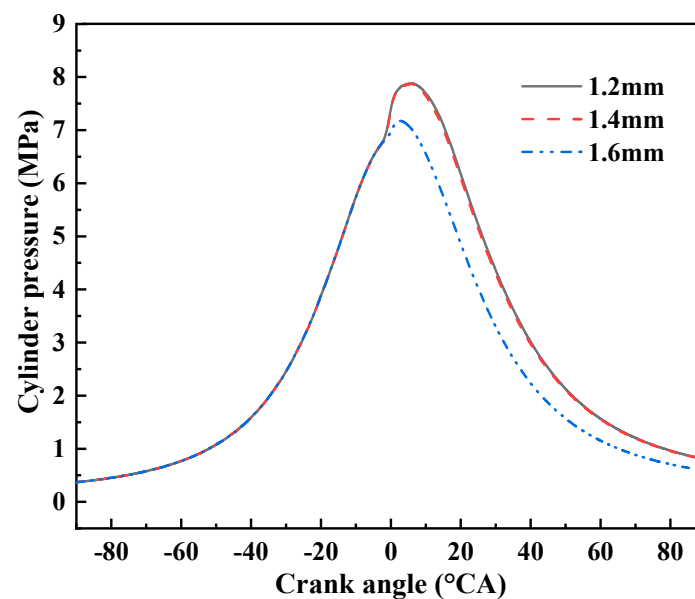


Figure 2. Comparison of the in-cylinder pressure curves of different basic grids.

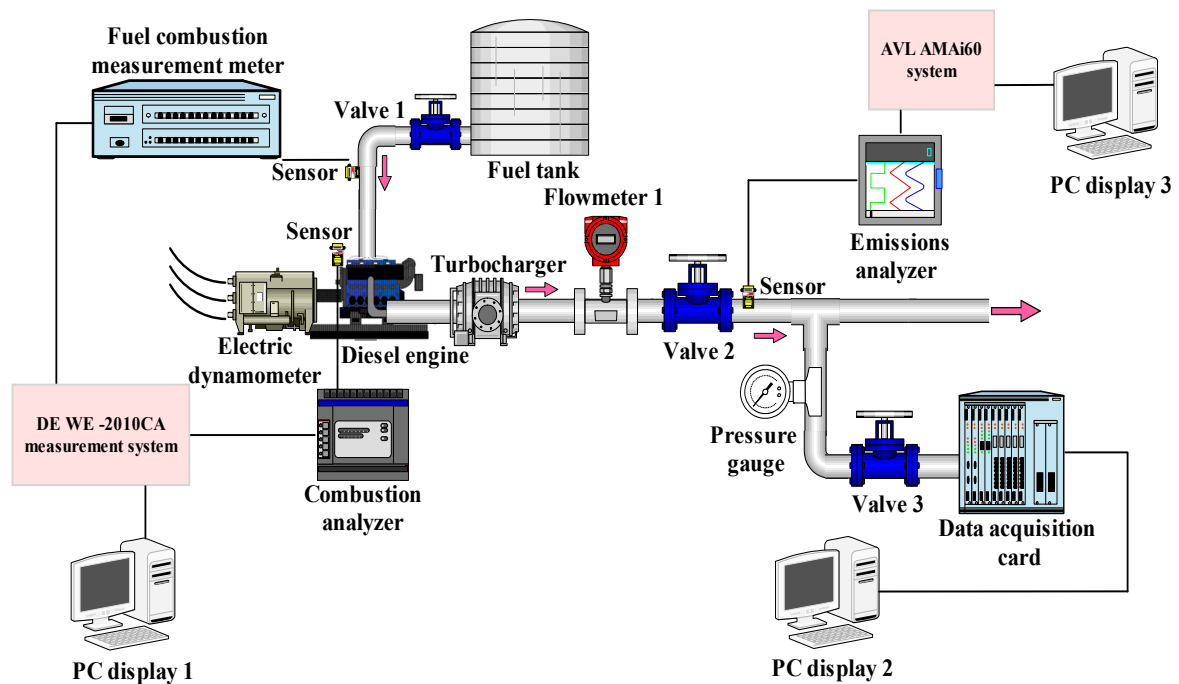
2.7. Engine Bench Test

This study investigated the combustion and emission characteristics of a diesel engine at a speed of 2000 rpm. Before the test, the engine was first warmed up in pure diesel fuel mode until the coolant temperature was between 65 and 85 °C. Then, all tests were arranged at an ambient temperature of about 25 °C. In addition, the intake air temperature after the intercooler was kept below 40 °C. When the engine was running in a stable condition in each test case, the in-cylinder pressure was recorded for 150 consecutive engine cycles and then averaged to ensure more accurate test results. At the same time, the exhaust gas from the engine was sampled using a probe, and then transmitted to an exhaust gas analyzer to obtain the composition of the exhaust gas, including soot, NO_x, HC, and CO.

Detailed physical properties of the fuel are shown in Table 2 [50–52]. The main specifications are listed in Table 1. The schematic diagram of the engine test is shown in Figure 3. The detailed specifications of the main measuring instruments are shown in Table 3.

Table 2. Fuel physical properties.

Performance Index	Diesel	Methanol	<i>n</i> -Butanol
Latent heat of gasification (kJ/kg)	260	1162.2	919.6
Density (kg/m ³) at 20 °C	835	792	810
Auto-ignition temperature (°C)	250	463	343
Low calorific value (MJ/kg)	42.5	20.1	30.63
Cetane number	51	3.8	17
Oxygen content (%) by weight	0	50	21.62
Stoichiometric air/fuel ratio	14.3	6.5	11.21
Kinematic viscosity (40 °C) (mm ² /s)	2.72	0.58	2.22

**Figure 3.** Schematic diagram of engine test.**Table 3.** Specifications of the main measuring instruments.

Item	Content	Accuracy	Uncertainty (%)
Electric dynamometer	NIDY S22-2/0525-1BV-1	Torque: $\pm 0.5\%$ F.S; Speed: ± 1 r/min	± 0.2
Dynamometer control system	PUMA OPEN1.4.1	$\pm 0.5\%$ F.S	± 0.2
Air flowmeter	TOCEIL 20N125	$\pm 1\%$	± 0.1
Diesel flowmeter	TOCEIL CMFG010	0.12%	± 0.2
Temperature sensor	Thermojunction type	± 0.5 °C	± 0.1
Pressure sensor	Piezoresistance type	$\pm 0.5\%$ F.S	± 0.5
Emissions analyzer	AVL AMAi60	$\pm 1.0\%$ F.S	± 0.2
Combustion analyzer	DEWE-2010CA	/	± 0.2
Injection measuring instrument	EFS-IFR600	$\pm 0.5\%$	± 0.5

2.8. Uncertainty Analysis

Generally, the experimental measurement results obtained have some errors and uncertainties [53]. The uncertainty of the experimental results is caused by the selection, observation, and calibration of sensors. The measurement results are used to calculate the required experimental results. The uncertainty percentage of parameters such as BSFC, BTE, and NO_x can be obtained from Equation (48). The *R* in Equation (49) is a function

of the independent variables I_1, I_2, \dots, I_n . Let u_1, u_2, \dots, u_n be the uncertainty in the independent variable and U_R be the uncertainty in the result.

$$U_R = \left\{ [(\partial R/\partial I_1)u_1]^2 + [(\partial R/\partial I_2)u_2]^2 + \dots + [(\partial R/\partial I_n)u_n]^2 \right\}^{1/2} \quad (48)$$

$$R = \{I_1, I_2, I_3, \dots, I_n\} \quad (49)$$

The measuring range and accuracy of the measuring equipment used in this paper are shown in Table 4. The following equation shows the calculated total experimental uncertainty.

$$\begin{aligned} &\text{Total uncertainty of the experiment} = \\ &\text{Square root of } [(\text{uncertainty of pressure sensor})^2 + (\text{uncertainty of HC emission})^2 \\ &+ (\text{uncertainty of NO}_x \text{ emission})^2 + (\text{uncertainty of CO emission})^2 \\ &+ (\text{uncertainty of Soot emission})^2] \\ &= \text{Square root of } [(0.5\%)^2 + (0.11\%)^2 + (0.53\%)^2 + (0.32\%)^2 + (2.8\%)^2] = 2.913\% \end{aligned}$$

Table 4. Uncertainty of measured parameters.

Measurements	Measuring Range	Accuracy	Uncertainty (%)
Engine speed	1–2000 rpm	±0.2%	±0.24
Pressure sensor	0–25 MPa	±10 kPa	±0.5
Exhaust gas temperature	0–1000 °C	±1 °C	±0.25
HC emission	0–20,000 ppm	±10 ppm	±0.11
NO _x emission	0–5000 ppm	±10 ppm	±0.53
CO emission	0–10% vol	±0.03%	±0.32
Soot emission	0–9 FSN	±0.1 FSN	±2.8
Air flow rate	0–33.3 kg/min	±1%	±0.5
Fuel flow rate	0.5–100 L/h	±0.04 L/h	±0.5

2.9. Model Validation

In order to verify the accuracy of the model, experiments were carried out. This paper validates the cylinder pressure (see Figure 4a) and heat release rate (see Figure 4b) of the combustion process and the NO_x and soot emissions of the emission process for the D70M20B10 (70% diesel, 20% methanol and 10% *n*-butanol by vol) blended fuel at 50% and 100% loads. Figure 4 shows the comparisons of the cylinder pressure and heat release rate at 100% and 50% loads, respectively. It was found that the experimental results were in good agreement with the simulation results. The maximum error was less than 4%. Thus, the results showed that the model could accurately simulate the in-cylinder combustion process. Figure 5 shows the simulation and experimental soot and NO_x emissions at 100% and 50% loads, respectively. It was found that the soot and NO_x emission trends were similar to the experiment. Therefore, this model can simulate the effect of pre-injection on combustion and emission characteristics.

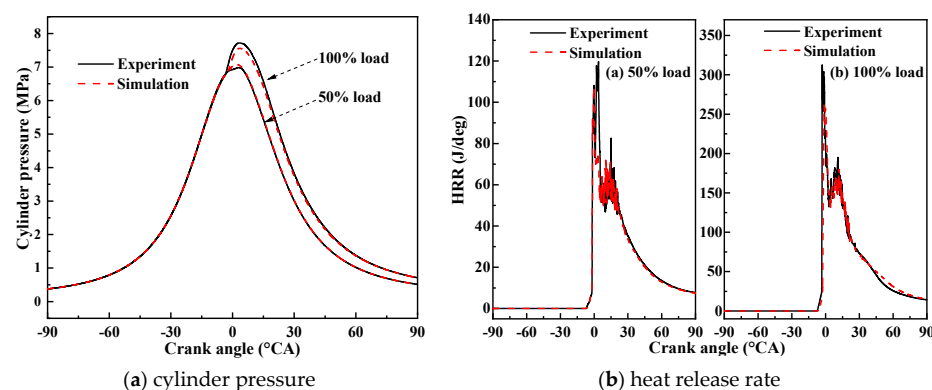


Figure 4. Engine validation results for cylinder pressure and heat release rate.

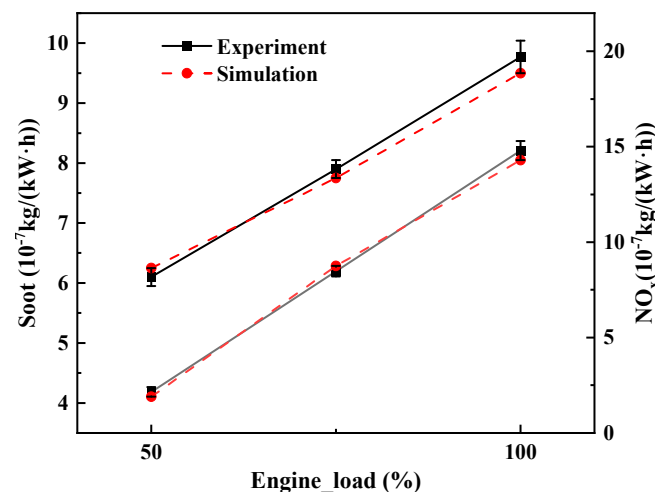


Figure 5. Engine validation results for soot and NO_x emissions.

3. Results and Discussions

To investigate the effects of the pre-injection timing and pre-injection mass ratio on the combustion and emission characteristics of the diesel engine, the CFD model was employed to simulate the combustion process. The specific pre-injection strategy parameters are shown in Table 5. The parameters defined in the pre-injection study are as follows. The start of pre-injection is defined as SOPI; the pre-injection mass ratio is defined as M_{pre} (where $M_{pre} = m_{pre}/(m_{main} + m_{pre})$); the start of the main injection is defined as SOMI; the main injection mass is defined as M_{main} (where $M_{main} = m_{main}/(m_{main} + m_{pre})$). The simulation results were then presented and analyzed in detail. Figure 6 shows the layout of the injector location in the CONVERGE environment.

Table 5. Parameters of the pre-injection strategy.

Case	Load (%)	SOPI (deg ATDC)	M_{pre}	SOMI (deg ATDC)	M_{main}
1	50	-	-	-9	1.0
2	50	-15~-45	0.5	-9	0.5
3	50	-45	0.1~0.9	-9	0.9~0.1
4	100	-	-	-9	1.0
5	100	-15~-45	0.5	-9	0.5
6	100	-45	0.1~0.9	-9	0.9~0.1

3.1. Combustion Analysis

3.1.1. Cylinder Pressure

Figure 7 shows comparisons of the cylinder pressure under different load conditions. Figure 7a,c shows that the cylinder pressure increases with the increase of SOPI. At 100% load, the maximum cylinder pressure at SOPI = -15, -25, -30, -35 and -45 °CA were 7.71, 9.46, 9.85, 9.912 and 9.95 MPa, respectively. The main reason is that the increase of SOPI leads to an advance of the combustion starting point, resulting in an increase of cylinder pressure. In addition, with the increase of SOPI, the turbulent kinetic energy in the combustion chamber increases, which increases the evaporation speed of the fuel and improves the in-cylinder combustion. Thus, the cylinder pressure increases. As shown in Figure 7b,d, the cylinder pressure increases with the increase of M_{pre} . At 100% load, the maximum cylinder pressures at $M_{pre} = 0.1, 0.3, 0.5, 0.7$ and 0.9 were 7.98, 9.10, 9.96, 10.52 and 11.16 MPa, respectively. This is because when SOPI remains unchanged, with the increase of M_{pre} , more fuel enters the cylinder earlier to participate in combustion, and more fuel is compressed during the compression stroke, increasing the cylinder pressure.

It can be seen that with the increase of SOPI and M_{pre} , the cylinder pressure of the diesel engine can be increased and the performance of the diesel engine can be improved.

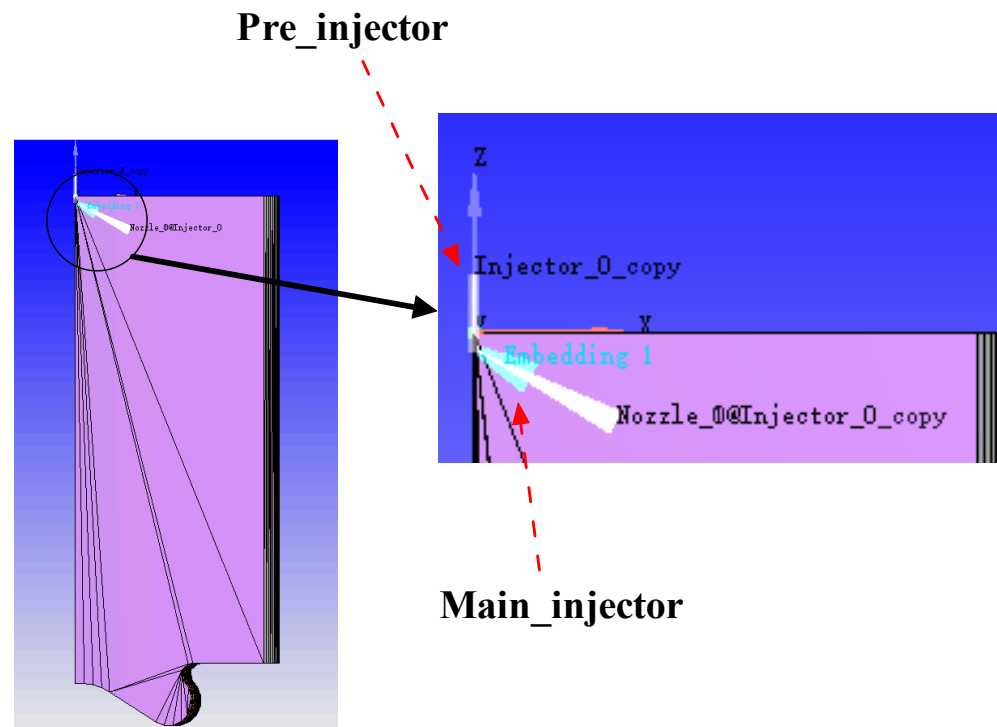


Figure 6. The layout of the injector location in the CONVERGE environment.

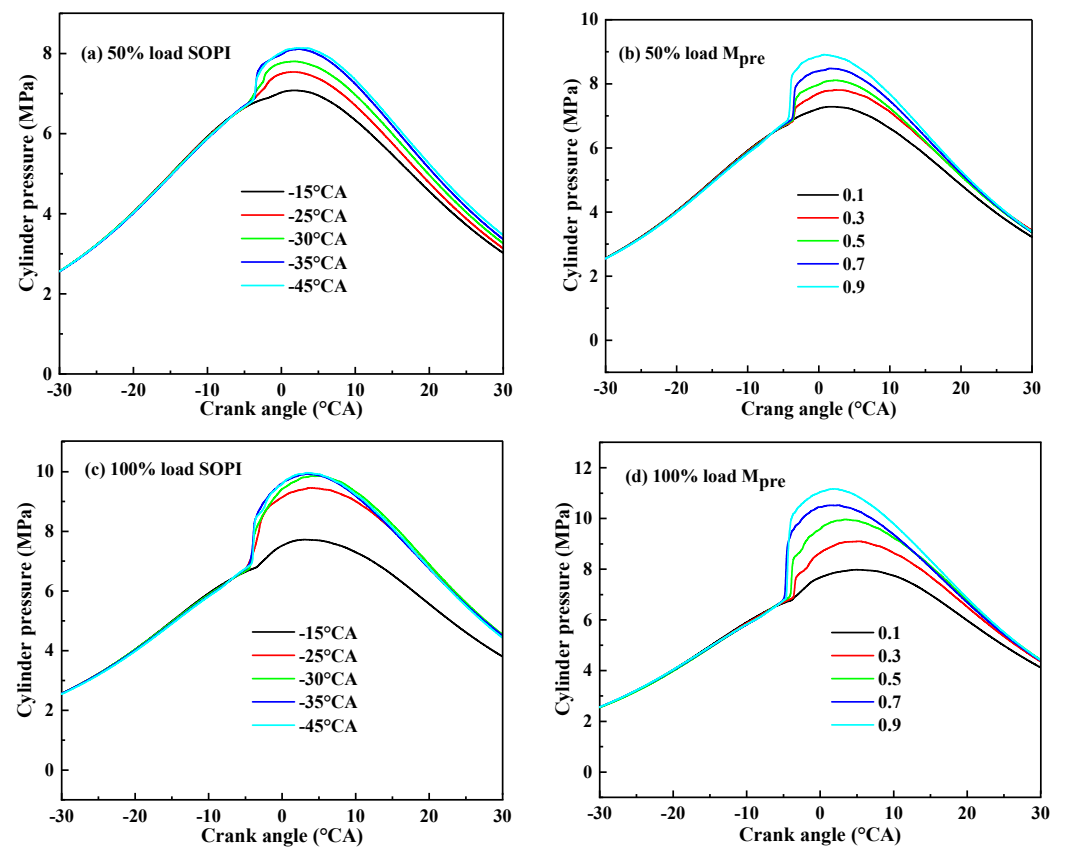


Figure 7. Comparisons of cylinder pressure under different load conditions.

3.1.2. Heat Release Rate (HRR)

Figure 8 shows comparisons of the HRR under different load conditions. As shown in Figure 8a,c, in all cases, the ignition delay was earliest at $\text{SOPI} = -15^\circ\text{CA}$, followed by -25 , -30 , -35 , and -45°CA . In addition, an increase of SOPI leads to an increase of the HRR peak and changes the HRR curve from a single peak to a double peak. This is because the increase of SOPI makes it easier to form a low concentration and homogeneous combustible mixture. This part of the mixture fails to fully release heat in the premixing stage, delaying the unburned blended fuel for the main injection stage and increasing the amount of fuel added to burn in the main injection stage. Therefore, the heat release rate of the main injection increases. As shown in Figure 8b,d, in all cases, the ignition delay was earliest at $M_{pre} = 0.9$, followed by 0.7, 0.5, 0.3, and 0.1. In addition, the heat release rate increases with the increase of M_{pre} . Due to the increase of M_{pre} , more fuel is compressed in the compression stroke, which accelerates the increase of the blended fuel temperature in the cylinder and improves the atomization and evaporation of the main injection diesel. Therefore, increasing HRR can significantly improve engine combustion characteristics.

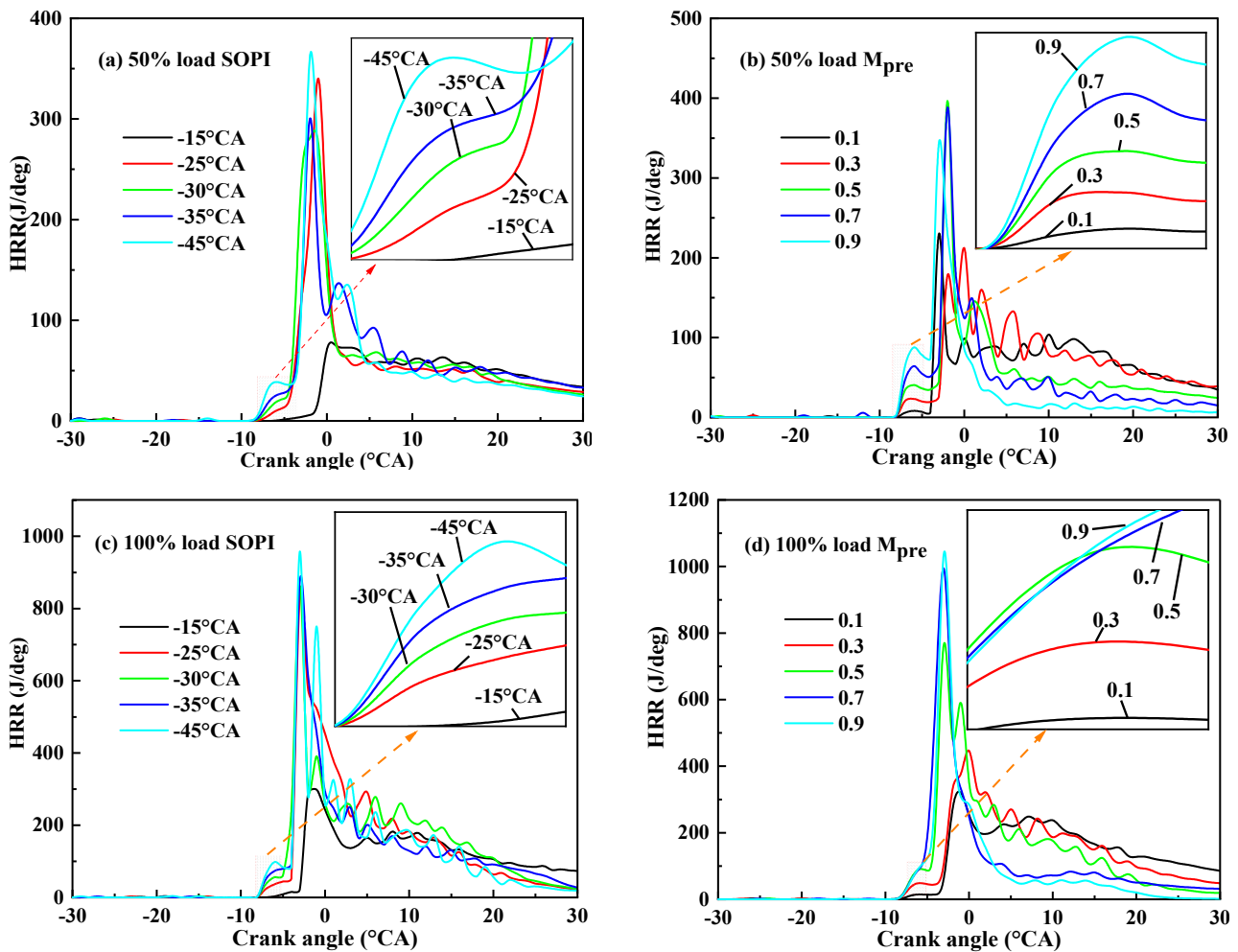


Figure 8. Comparison of HRR under different load conditions.

3.1.3. Cylinder Temperature

Figure 9 shows the comparisons of in-cylinder temperature under different load conditions. It can be seen that the cylinder temperature increases with the increase of SOPI and M_{pre} . At 50% load, the maximum cylinder temperature at $\text{SOPI} = -15$, -25 , -30 , -35 and -45°CA were 953.20, 1005.23, 1042.02, 1091.15 and 1102.46 K, respectively; the maximum cylinder temperatures at $M_{pre} = 0.1$, 0.3, 0.5, 0.7 and 0.9 were 984.04, 1062.51,

1091.16, 1134.54 and 1180.21 K, respectively. This is mainly because with the increase of SOPI and M_{pre} , the ignition delay period of the combustion process is prolonged, and the fuel is fully blended, which increases the combustion speed of the fuel, resulting in more heat release, thus increasing the temperature in the cylinder. In addition, with the increase of SOPI and M_{pre} , the cold flame effect is enhanced, and the temperature in the cylinder is increased.

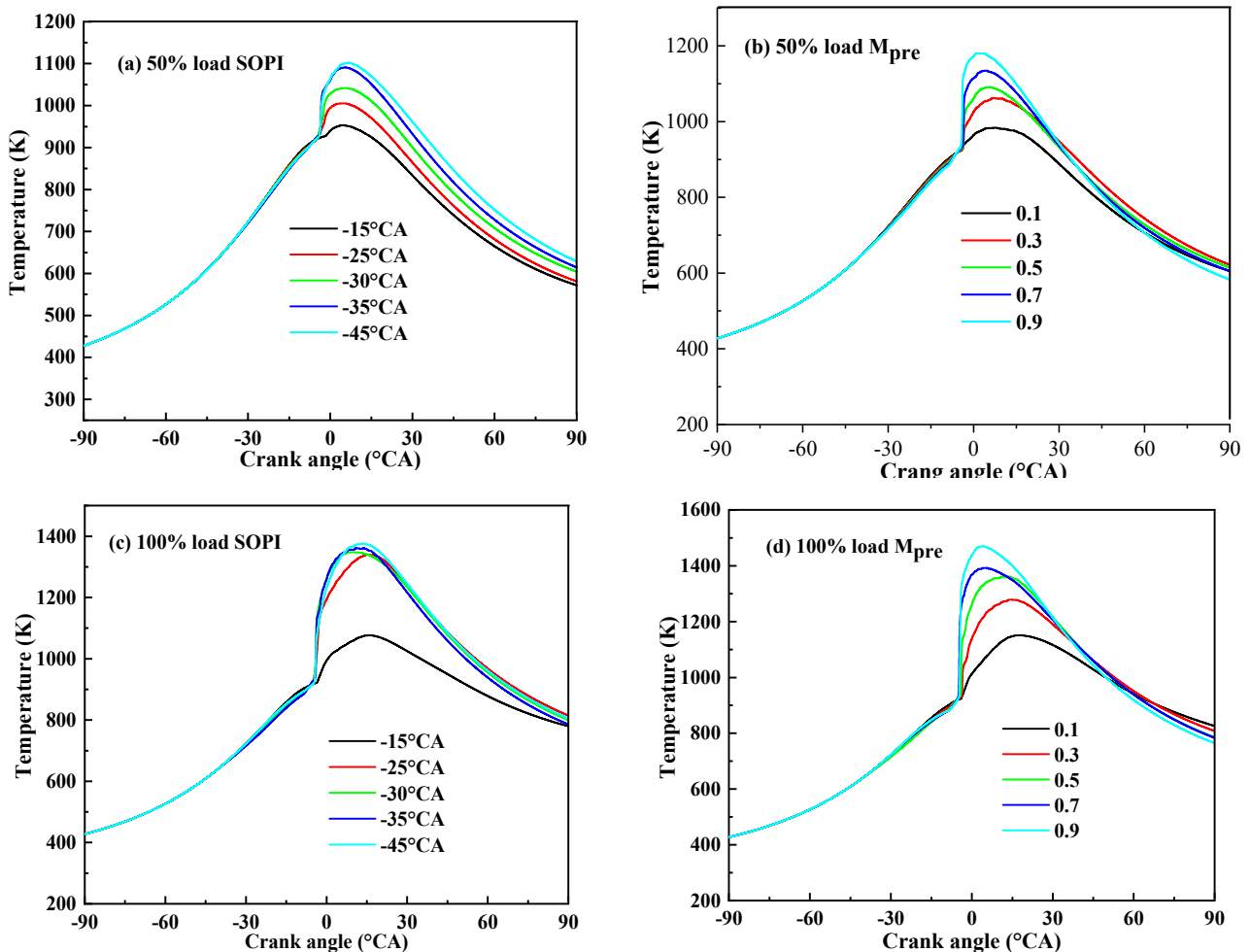


Figure 9. Comparisons of cylinder temperature changes under different load conditions.

Figure 10 shows the temperature distribution field under different load conditions. It can be seen that when the pre-injection strategy is adopted, the high-temperature area increases with the increase of SOPI and M_{pre} . When $TDC = -5$ °CA, the temperature of the newly injected fuel was low, which cooled the injection area of the combustion chamber. When $TDC = 1$ °CA, the temperature in the cylinder increases due to fuel combustion, especially at the front end of the fuel beam, where combustion occurs first. When $TDC = 7$ °CA, the temperature in the cylinder continues to increase with the progress of combustion, and the maximum temperature in the cylinder increases with the increase of SOPI. In addition, when SOPI = -15 °CA or -25 °CA and $M_{pre} = 0.1$ or 0.3 , the temperature distribution in the cylinder was uneven. At SOPI = -30 , -35 , and -45 °CA and $M_{pre} = 0.5$, 0.7 , and 0.9 , the combustion conditions were better because of a longer fuel ignition delay and sufficient fuel blending. Thus, the in-cylinder temperature was also more evenly distributed. Therefore, increasing SOPI and M_{pre} within a certain range are more conducive to fuel combustion.

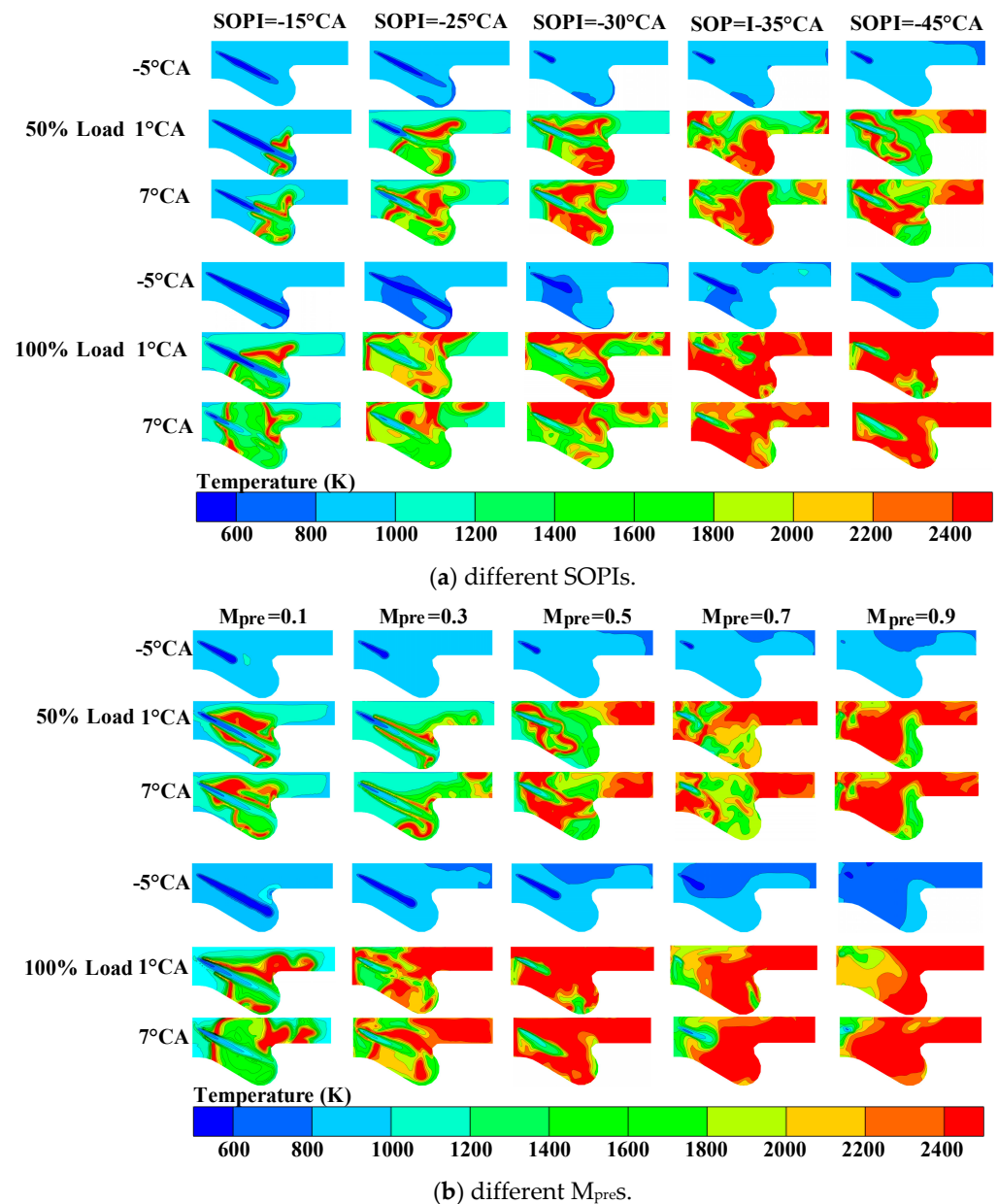


Figure 10. Comparisons of the cylinder temperature distribution field under different load conditions.

In addition, the generation of NO_x in the cylinder is closely related to the temperature. If the temperature in the cylinder is too high it will increase the emission of NO_x . Therefore, SOPI and M_{pre} should be reasonably selected to reduce the emission.

3.2. Emissions Analysis

3.2.1. Soot Emission

Figure 11 shows the comparison of soot changes under different load conditions. As shown in Figure 11a,c, with the increase of SOPI, the soot emission shows a downward trend. At 50% load, the soot emission at SOPI = -15, -25, -30, -35 and -45 °CA were decreased by 7.30%, 9.45%, 27.70%, 66.80% and 81.80%, respectively. Moreover, with the increase of M_{pre} , soot emission decreases. At 50% load, the soot emission at $M_{pre} = 0.1, 0.3, 0.5, 0.7$ and 0.9 were decreased by 11.30%, 20.03%, 71.32%, 83.80% and 93.76%, respectively. The main reason is that with the increase of SOPI and M_{pre} , the temperature in the combustion chamber increases, and the cold flame effect caused by pre-injection combustion is enhanced, resulting in the main injection combustion conditions

being improved and so the combustion speed is accelerated. The formation condition of soot is a high temperature and anoxic environment, which is the product of an incomplete combustion of fuel and has a trade-off relationship with NO_x [54]. With the increase of SOPI and M_{pre} , the area of an equivalent ratio in the combustion chamber decreases, the in-cylinder combustion conditions are improved to a certain extent, the combustion is more complete, and the formation of soot decreases. However, in Figure 10c,d, the soot emission firstly increases and then decreases. The reason is that at SOPI = -15°CA and $M_{pre} = 0.1$, the cylinder pressure and cylinder temperature are low (as shown in Figures 7 and 9), resulting in incomplete combustion of the fuel, which increases soot emission. In summary, a reasonable SOPI and M_{pre} can decrease soot emission.

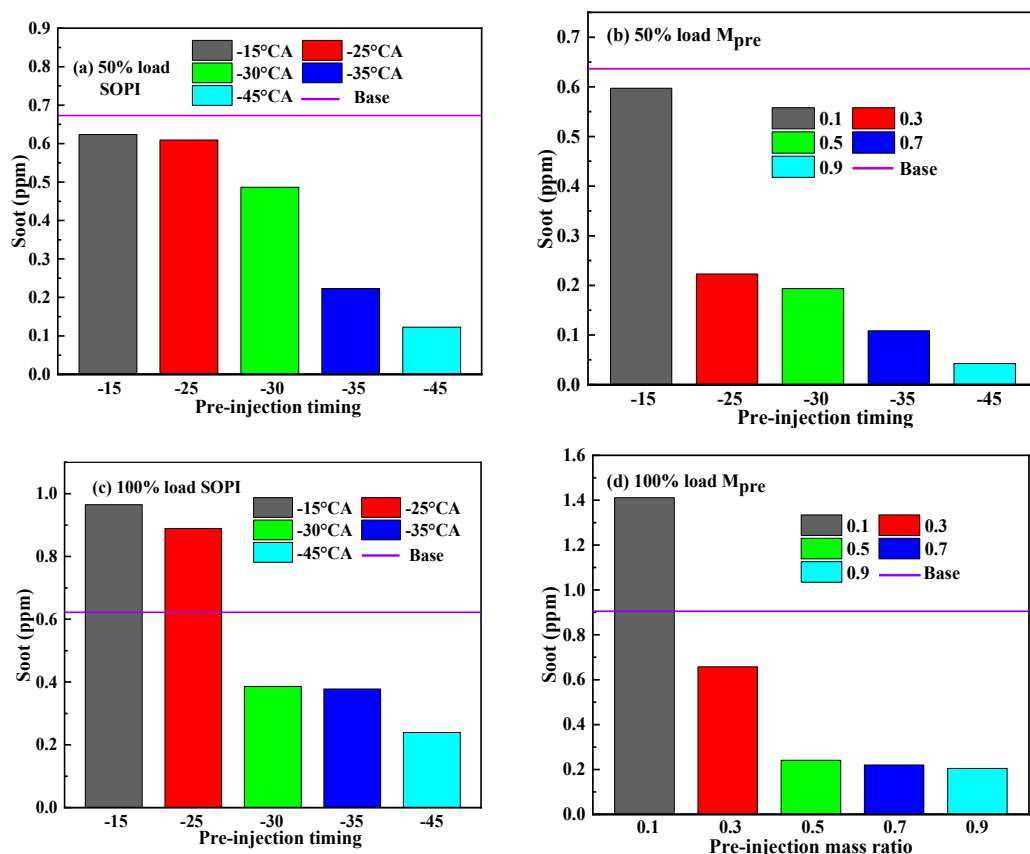


Figure 11. Comparisons of soot emission under different load conditions.

3.2.2. NO_x Emission

Figure 12 shows the comparison of NO_x changes under different load conditions. As shown in the figure, NO_x emission increases with the increase of SOPI and M_{pre} . In all cases, the NO_x emission was highest at SOPI = -45°CA and $M_{pre} = 0.9$, followed by SOPI = $-25, -30, -35, -45^\circ\text{CA}$ and $M_{pre} = 0.7, 0.5, 0.3, 0.1$. The main reason is that when SOPI increases, the temperature in the combustion chamber increases, and the cold flame effect caused by pre-injection combustion increases, resulting in the main injection combustion conditions being improved, a faster combustion speed, and a higher combustion temperature. When M_{pre} increases, the blended fuel in the combustion chamber increases, and the fuel blends more fully, increasing the cylinder temperature. Moreover, NO_x is produced under the conditions of a high-temperature oxygen-enriched environment and high-temperature duration. Therefore, when the speed remains unchanged, the temperature in the cylinder increases, which will increase NO_x emission. It can be seen that an increase of SOPI and M_{pre} is not good for NO_x emission, and a reasonable SOPI and M_{pre} can improve the performance of the diesel engine. However, diesel engine emissions should also be considered at the same time.

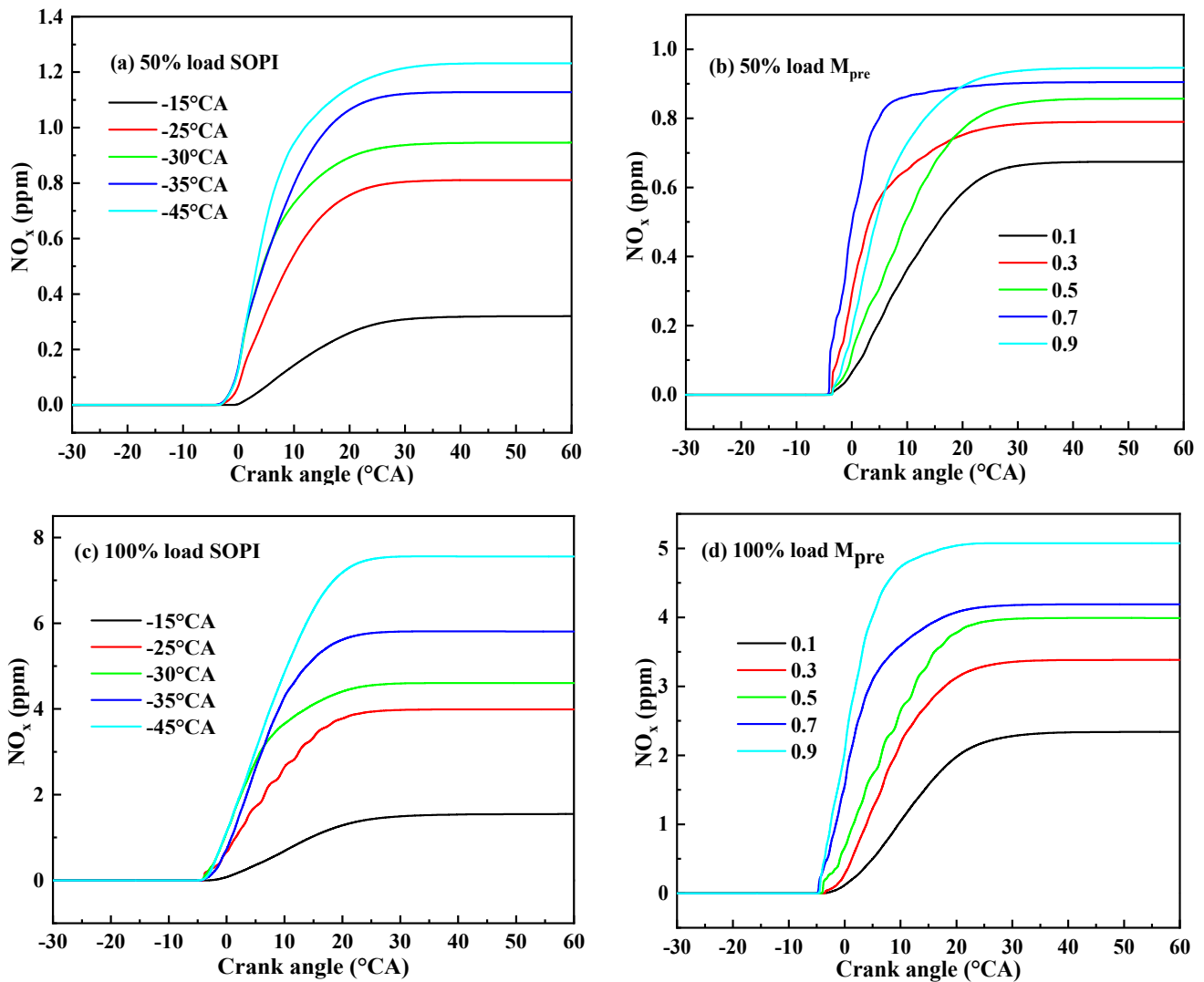


Figure 12. Comparisons of NO_x emission under different load conditions.

Figure 13 shows the NO_x distribution under different conditions. As shown in the figure, at $\text{TDC} = -5^\circ\text{CA}$, only a small amount of NO_x is formed due to in-cylinder combustion and the effect of waste heat in the cylinder. When $\text{TDC} = 1^\circ\text{CA}$, NO_x is mainly generated in the high-temperature area at the front of the fuel beam because the formation of NO_x is affected by high temperatures. When $\text{TDC} = 7^\circ\text{CA}$, with the progress of combustion, the high-temperature area gradually diffuses into the whole cylinder, and the NO_x formation area increases and diffuses into the whole combustion chamber. As shown in Figures 12 and 13, the NO_x distribution area of the combustion chamber is consistent with the temperature, indicating that the temperature is an important factor affecting NO_x .

3.2.3. HC Emission

Figure 14 shows the change of HC under different load conditions. It can be seen that with SOPI increases, HC emissions firstly increase and then decrease. At 50% load, the HC emission at SOPI = -15 , -25 , -30 , -35 and -45°CA changed by $+42.81\%$, -7.94% , -30.22% , -35.75% and -41.24% , respectively. As shown in Figures 7 and 9, when SOPI = -15°CA , the cylinder pressure and cylinder temperature are low, resulting in incomplete combustion of the fuel, which increases HC emissions. With an increase of SOPI, the ignition delay of the pilot diesel increases, and more combustible blended fuel can

be obtained. The combustion has more ignition points and ignition energy to improve the combustion, resulting in an increase of temperature and pressure in the cylinder, and the fuel combustion is more complete. At the same time, the earlier injection moment will make the combustion start earlier, and the HC formed by combustion will have adequate time for oxidation reactions so that HC emissions will be decreased. In addition, with the increase of M_{pre} , HC emission increases first and then decreases. At 50% load, the HC emission at $M_{pre} = 0.1, 0.3, 0.5, 0.7$ and 0.9 changed by $+12.71\%, -28.02\%, -36.74\%, -59.43\%$ and -82.71% , respectively. When $M_{pre} = 0.1$, less fuel enters the cylinder. Moreover, as shown in Figures 7 and 9, the cylinder pressure and cylinder temperature are low, resulting in incomplete combustion of the fuel, which increases HC emissions. With M_{pre} continuing to increase, the HC emissions decrease. This may be because as the fuel increases, it makes the combustion more complete. The earlier SOPI and larger M_{pre} can significantly decrease HC emissions, which is important for the diesel engine.

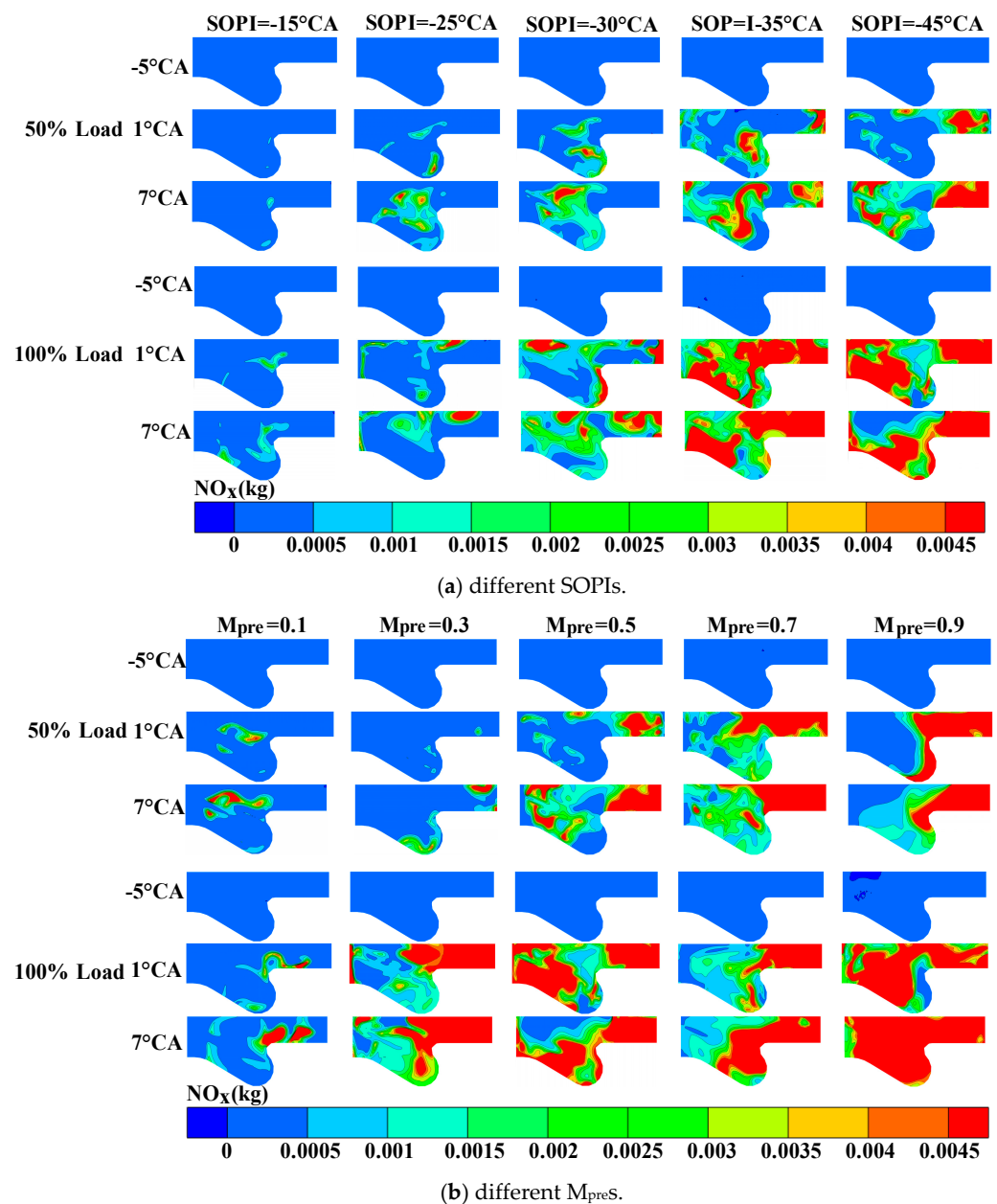


Figure 13. Comparison of NO_x distribution field changes under different load conditions.

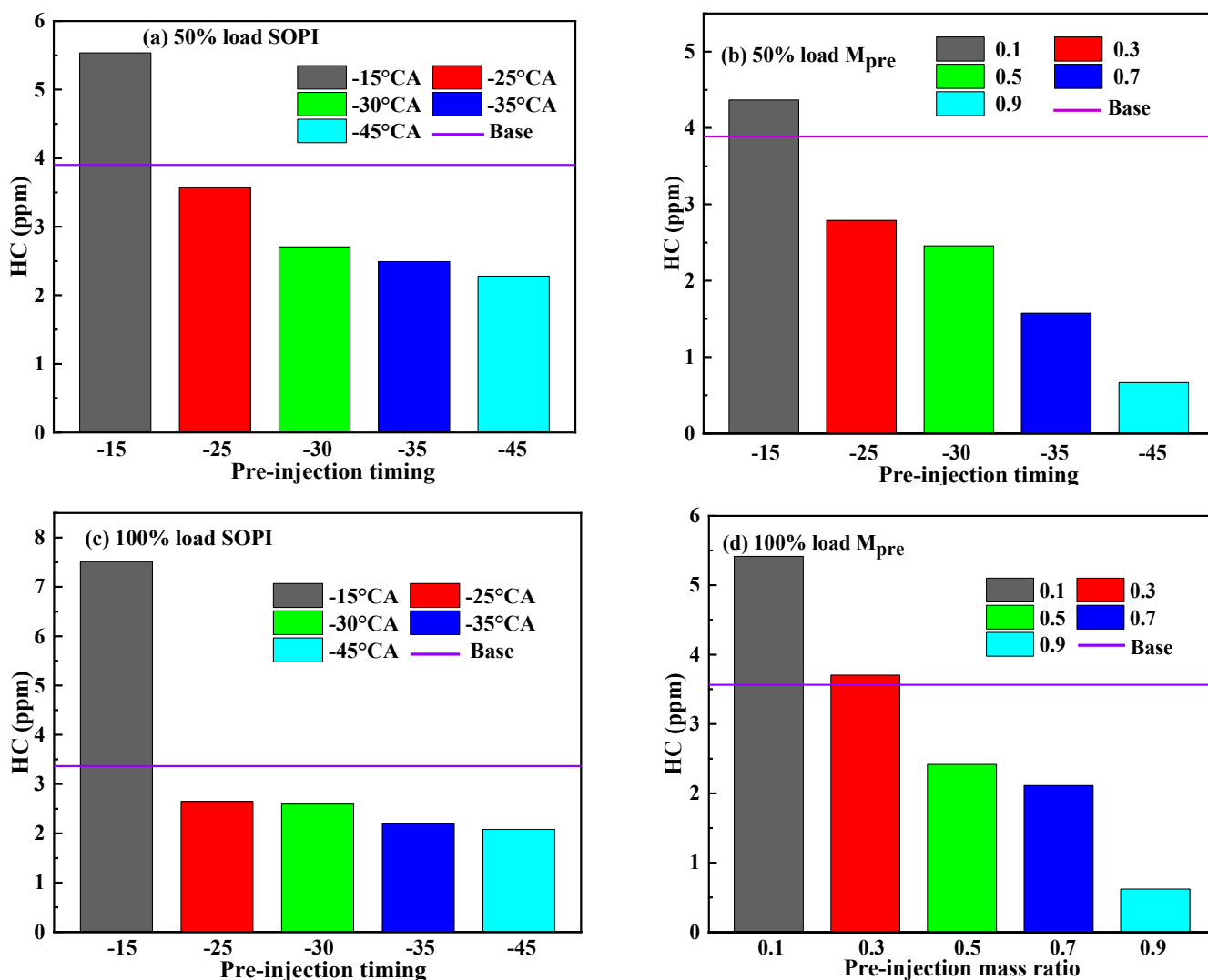


Figure 14. Comparison of HC changes under different load conditions.

3.2.4. CO Emission

CO emission is mainly caused by incomplete combustion. In addition, carbon dioxide (CO_2) cracking under a high-temperature environment in the cylinder is another important reason [55]. Figure 15 shows the change of CO percentage under different load conditions. It can be seen that CO emissions decrease with the increase of SOPI and M_{pre} . Taking 50% load as an example, with the increase of SOPI, CO emission changed by -5.77% , -12.31% , -22.73% , -53.59% , and -63.22% , respectively. With the increase of M_{pre} , CO emission changed by -8.29% , -43.97% , -53.59% , -58.86% , and -61.18% , respectively. This may be due to the increase of SOPI, so the time for evaporation and fuel blending are enough to completely burn it. In addition, due to the increase of M_{pre} , more fuel is provided for combustion. Therefore, CO emission is decreased. In addition, a larger SOPI and M_{pre} will prolong the blending time of fuel and air to decrease CO emission. It can be seen that increases of SOPI and M_{pre} can significantly decrease the emission of CO.

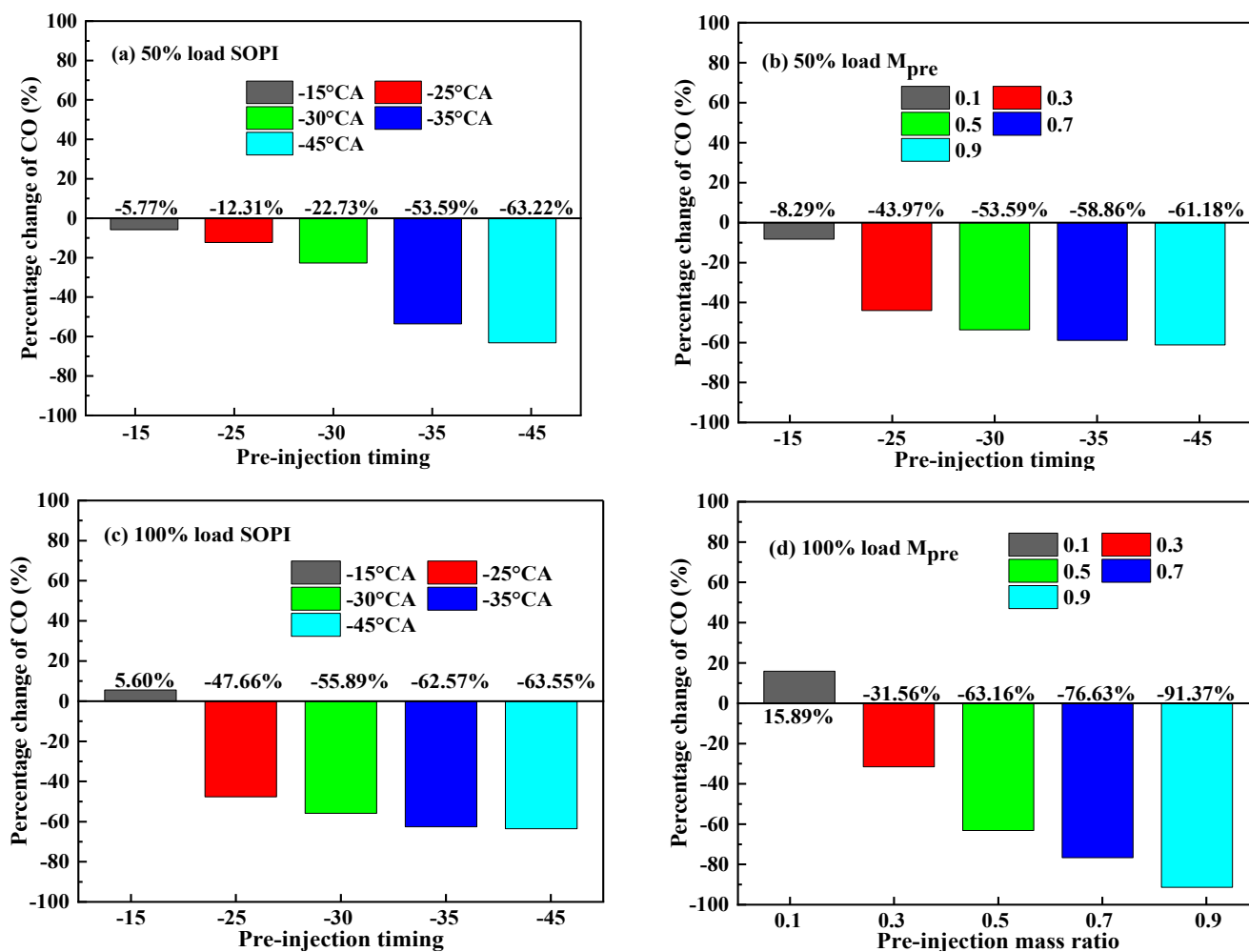


Figure 15. Comparison of the CO percentage change under different load conditions.

4. Conclusions

Due to the global energy crisis [56–60] and environmental problems [61–66], the development of diesel engines is also facing great challenges. In this paper, it is studied the effects of pre-injection timing and pre-injection mass ratio on the combustion and emission characteristics of a diesel/methanol/*n*-butanol blended fuel engine using computational fluid dynamics and a chemical dynamics model. The 3-D CFD simulation model was established and calibrated based on the test data under the two typical working conditions [67,68]. The intermediate process of combustion and emission can be easily obtained and used to explain the changes of combustion and emission parameters through the simplified chemical kinetic model. Through the analysis of experimental data and simulation results, the following conclusions are drawn:

- (1) When the pre-injection timing changes from -15°CA to -45°CA , the engine cylinder pressure increases, and the cylinder temperature increases. The increase in SOPI leads to an earlier start of combustion, which increases the evaporation rate of the fuel and improves in-cylinder combustion.
- (2) When the pre-injection fuel mass ratio changes from 0.1 to 0.9, the engine cylinder pressure increases and the cylinder temperature increases. This is because with the increase of M_{pre} , more fuel enters the cylinder in advance to participate in combustion, and more fuel is compressed in the compression stroke, resulting in more heat release, thus increasing cylinder pressure and cylinder temperature.

- (3) With the increase of SOPI, soot, CO and HC emissions are decreased. This is because with the increase of SOPI, more combustible blended fuels can be obtained, and the time for fuel evaporation and fuel blending is enough to make it burn completely.
- (4) With the increase of M_{pre} , soot, CO and HC emissions are reduced. With the increase of M_{pre} , more fuel is used to participate in combustion, making the combustion more complete.
- (5) NO_x emission increases with SOPI and M_{pre} . NO_x is produced under high-temperature oxygen-rich environments and high-temperature duration conditions. Therefore, the temperature in the cylinder increases, which will increase NO_x emission.

From the present work, it can be concluded that the diesel engine fueled with diesel/methanol/*n*-butanol blends, combined with a pre-injection strategy can significantly improve diesel combustion performance and decrease emissions. Therefore, to balance the emissions of NO_x , HC, CO, and soot, the optimal pre-injection timing and the optimal pre-injection mass ratio should be $\text{SOPI} = -30^\circ\text{CA}$ and $M_{pre} = 0.5$.

Author Contributions: Conceptualization, Z.W. and L.L.; software, Z.W.; formal analysis, Z.W. and L.L.; investigation, Z.W. and L.L.; resources, L.L.; writing—original draft preparation, Z.W.; writing—review and editing, Z.W. and L.L.; supervision, L.L.; funding acquisition, Z.W. and L.L. All authors have read and agreed to the published version of the manuscript.

Funding: This research was funded by the key research and development project of Hunan Province (2021NK2023) and the Special funds for the construction of the innovative Hunan Province (2019NK2022).

Data Availability Statement: All data used to support the findings of this study are included within the article.

Conflicts of Interest: The authors declare that they have no conflict of interest regarding the publication of this paper.

References

1. Viswanathan, K.; Subramanian, T.; Ashok, B.; Varuvel, E.; Azad, K. Experimental investigation of pomegranate oil methyl ester in ceramic coated engine at different operating condition in direct injection diesel engine with energy and exergy analysis. *Energy Convers. Manag.* **2020**, *205*, 112334.
2. Tan, D.; Chen, Z.; Li, J.; Luo, J.; Yang, D.; Cui, S.; Zhang, Z. Effects of Swirl and Boiling Heat Transfer on the Performance Enhancement and Emission Reduction for a Medium Diesel Engine Fueled with Biodiesel. *Processes* **2021**, *9*, 568. [[CrossRef](#)]
3. Zhang, Z.; Ye, J.; Tan, D.; Feng, Z.; Luo, J.; Tan, Y.; Huang, Y. The effects of Fe_2O_3 based DOC and SCR catalyst on the combustion and emission characteristics of a diesel engine fueled with biodiesel. *Fuel* **2021**, *290*, 120039. [[CrossRef](#)]
4. Nanthagopal, K.; Ashok, B.; Tamilarasu, A.; Johnny, A.; Mohan, A. Influence on the effect of zinc oxide and titanium dioxide nanoparticles as an additive with *Calophyllum inophyllum* methyl ester in a CI engine. *Energy Convers. Manag.* **2017**, *146*, 8–19. [[CrossRef](#)]
5. E, J.; Zhang, Z.; Chen, J.; Pham, M.; Zhao, X.; Peng, Q.; Zhang, B.; Yin, Z. Performance and emission evaluation of a marine diesel engine fueled by water biodiesel-diesel emulsion blends with a fuel additive of a cerium oxide nanoparticle. *Energy Convers. Manag.* **2018**, *169*, 194–205. [[CrossRef](#)]
6. Zhang, Z.; Chen, J.; Zhu, H.; Zhao, X.; Han, D.; Zuo, W.; Peng, Q.; Gong, J.; Yin, Z. Effects of low-level water addition on spray, combustion and emission characteristics of a medium speed diesel engine fueled with biodiesel fuel. *Fuel* **2019**, *239*, 245–262. [[CrossRef](#)]
7. E, J.; Zhao, X.; Qiu, L.; Wei, K.; Zhang, Z.; Deng, Y.; Han, D.; Liu, G. Experimental investigation on performance and economy characteristics of a diesel engine with variable nozzle turbocharger and its application in urban bus. *Energy Convers. Manag.* **2019**, *193*, 149–161. [[CrossRef](#)]
8. Zhang, Z.; E, J.; Chen, J.; Zhao, X.; Zhang, B.; Deng, Y.; Peng, Q.; Yin, Z. Effects of boiling heat transfer on the performance enhancement of a medium speed diesel engine fueled with diesel and rapeseed methyl ester. *Appl. Therm. Eng.* **2020**, *169*, 114984. [[CrossRef](#)]
9. Saiteja, P.; Ashok, B. A critical insight review on homogeneous charge compression ignition engine characteristics powered by biofuels. *Fuel* **2021**, *285*, 119202. [[CrossRef](#)]
10. Viswanathan, K.; Ashok, B.; Nanthagopal, K.; Subramanian, T.; Varuvel, E. Investigation of Novel Pistacia khinjuk Biodiesel in DI Diesel Engine with Post Combustion Capture System. *Appl. Therm. Eng.* **2019**, *159*, 113969.
11. Viswanathan, K.; Subramanian, T.; Varuvel, E.; Ashok, B.; Nanthagopal, K.; Ong, H.C.; Rajasekar, V. Simultaneous reduction of NO_x and smoke emissions with low viscous biofuel in low heat rejection engine using selective catalytic reduction technique. *Fuel* **2019**, *255*, 115854.

12. Chen, Z.; He, J.; Chen, H.; Geng, L.; Zhang, P. Comparative study on the combustion and emissions of dual-fuel common rail engines fueled with diesel/methanol, diesel/ethanol, and diesel/*n*-butanol. *Fuel* **2021**, *304*, 121360. [[CrossRef](#)]
13. Hasan, A.O.; Osman, A.I.; Al-Muhtaseb, A.H.; Al-Rawashdeh, H.; Abu-jrai, A.; Ahmad, R.; Gomaa, M.R.; Deka, T.J.; Rooney, D.W. An experimental study of engine characteristics and tailpipe emissions from modern DI diesel engine fuelled with methanol/diesel blends. *Fuel Process. Technol.* **2021**, *220*, 106901. [[CrossRef](#)]
14. Li, Z.; Wang, Y.; Yin, Z.; Gao, Z.; Wang, Y.; Zhen, X. Parametric study of a single-channel diesel/methanol dual-fuel injector on a diesel engine fueled with directly injected methanol and pilot diesel. *Fuel* **2021**, *302*, 121156. [[CrossRef](#)]
15. Park, S.; Jungkeun, C.; Park, J.; Song, S. Numerical study of the performance and NO_x emission of a diesel-methanol dual-fuel engine using multi-objective Pareto optimization. *Energy* **2017**, *124*, 272–283. [[CrossRef](#)]
16. Zhang, Z.; Tian, J.; Li, J.; Ji, H.; Tan, D.; Luo, J.; Jiang, Y.; Yang, D.; Cui, S. Effects of Different Mixture Ratios of Methanol-Diesel on the Performance Enhancement and Emission Reduction for a Diesel Engine. *Processes* **2021**, *9*, 1366. [[CrossRef](#)]
17. Ning, L.; Duan, Q.; Kou, H.; Zeng, K. Parametric study on effects of methanol injection timing and methanol substitution percentage on combustion and emissions of methanol/diesel dual-fuel direct injection engine at full load. *Fuel* **2020**, *279*, 118424. [[CrossRef](#)]
18. Yilmaz, N.; Sanchez, T. Analysis of operating a diesel engine on biodiesel-ethanol and biodiesel-methanol blends. *Energy* **2012**, *46*, 126–129. [[CrossRef](#)]
19. Ning, L.; Duan, Q.; Zhanming, C.; Kou, H.; Liu, B.; Yang, B.; Zeng, K. A comparative study on the combustion and emissions of a non-road common rail diesel engine fueled with primary alcohol fuels (methanol, ethanol, and *n*-butanol)/diesel dual fuel. *Fuel* **2020**, *266*, 117034. [[CrossRef](#)]
20. Jin, C.; Yao, M.; Liu, H.; Lee, C.-f.; Ji, J. Progress in the production and application of *n*-Butanol as a biofuel. *Renew. Sustain. Energy Rev.* **2011**, *15*, 4080–4106. [[CrossRef](#)]
21. Nanthagopal, K.; Kishna, R.; Atabani, A.; Al-Muhtaseb, A.H.; Kumar, G.; Ashok, B. A compressive review on the effects of alcohols and nanoparticles as an oxygenated enhancer in compression ignition engine. *Energy Convers. Manag.* **2019**, *203*, 112244. [[CrossRef](#)]
22. Szabados, G.; Lukács, K.; Bereczky, A. Investigating Combustion Process of *N*-Butanol-Diesel Blends in a Diesel Engine with Variable Compression Ratio. *Clean Technol.* **2021**, *3*, 618–628. [[CrossRef](#)]
23. Satsangi, D.; Tiwari, N. Experimental investigation on combustion, noise, vibrations, performance and emissions characteristics of diesel/*n*-butanol blends driven genset engine. *Fuel* **2018**, *221*, 44–60. [[CrossRef](#)]
24. Rakopoulos, D.; Rakopoulos, C.; Giakoumis, E.; Dimaratos, A.; Kyritsis, D. Effects of butanol–diesel fuel blends on the performance and emissions of a high-speed DI diesel engine. *Energy Convers. Manag.* **2010**, *51*, 1989–1997. [[CrossRef](#)]
25. Ashok, B.; Ashok, S.; Kumar, C. LPG diesel dual fuel engine—A critical review. *Alex. Eng. J.* **2015**, *36*, 105–126. [[CrossRef](#)]
26. Mobasher, R.; Peng, Z.; Mirsalim, S. Analysis the effect of advanced injection strategies on engine performance and pollutant emissions in a heavy duty DI-diesel engine by CFD modeling. *Int. J. Heat Fluid Flow* **2011**, *33*, 59–69. [[CrossRef](#)]
27. Lu, Y.; Liu, Y. Effects of multiple injections on combustion and emissions in a heavy-duty diesel engine at high load and low speed. *Adv. Mech. Eng.* **2020**, *12*, 1–15. [[CrossRef](#)]
28. Wang, H.; Gan, H.; Theotokatos, G. Parametric investigation of pre-injection on the combustion, knocking and emissions behaviour of a large marine four-stroke dual-fuel engine. *Fuel* **2020**, *281*, 118744. [[CrossRef](#)]
29. Liu, J.; Yao, A.; Yao, C. Effects of injection timing on performance and emissions of a HD diesel engine with DMCC. *Fuel* **2014**, *134*, 107–113. [[CrossRef](#)]
30. Liu, B.; Cheng, X.; Liu, J.; Pu, H. Investigation into particle emission characteristics of partially premixed combustion fueled with high *n*-butanol-diesel ratio blends. *Fuel* **2018**, *223*, 1–11. [[CrossRef](#)]
31. Bhowmick, P.; Jeevanantham, A.K.; Ashok, B.; Nanthagopal, K.; Perumal, D.D.A.; Viswanathan, K.; Vora, K.C.; Jain, A. Effect of Fuel Injection Strategies and EGR on Biodiesel Blend in a CRDI engine. *Energy* **2019**, *181*, 1094–1113. [[CrossRef](#)]
32. Paykani, A.; Kakaee, A.; Rahnama, P.; Reitz, R. Effects of diesel injection strategy on natural gas/diesel reactivity controlled compression ignition combustion. *Energy* **2015**, *90*, 814–826. [[CrossRef](#)]
33. Jiang, X.; Wei, H.; Zhou, L.; Chen, R. Numerical Study on the Effects of Multiple-Injection Coupled with EGR on Combustion and NO_x Emissions in a Marine Diesel Engine. *Energy Procedia* **2019**, *158*, 4429–4434. [[CrossRef](#)]
34. Liu, T.; E, J.; Yang, W.M.; Deng, Y.; An, H.; Zhang, Z.; Pham, M. Investigation on the applicability for adjusting reaction rates of the optimized biodiesel skeletal mechanism. *Energy* **2018**, *150*, 1031–1038. [[CrossRef](#)]
35. Zhang, Z.; Li, J.; Tian, J.; Xie, G.; Tan, D.; Qin, B.; Huang, Y.; Cui, S. Effects of Different Diesel-Ethanol Dual Fuel Ratio on Performance and Emission Characteristics of Diesel Engine. *Processes* **2021**, *9*, 1135. [[CrossRef](#)]
36. Gong, C.; Liu, J.; Peng, L.; Liu, F. Numerical study of effect of injection and ignition timings on combustion and unregulated emissions of DISI methanol engine during cold start. *Renew. Energy* **2017**, *112*, 457–465. [[CrossRef](#)]
37. Zang, R.; Yao, C. Numerical Study of Combustion and Emission Characteristics of a Diesel/Methanol Dual Fuel (DMDF) Engine. *Energy Fuel* **2015**, *29*, 3963–3971. [[CrossRef](#)]
38. Wang, C.H.; Zhao, D.; Schluter, J.; Holzäpfel, F.; Stephan, A. LES study on the shape effect of ground obstacles on wake vortex dissipation. *Aerosp. Sci. Technol.* **2017**, *63*, 245–258. [[CrossRef](#)]
39. Han, Z.; Reitz, R. Turbulence Modeling of Internal Combustion Engines Using RNG κ - ϵ Models. *Combust. Sci. Technol.* **1995**, *106*, 267–295. [[CrossRef](#)]

40. Yakhot, V.; Orszag, S.A.; Thangam, S.; Gatski, T.; Speziale, C. Development of Turbulence Models for Shear Flows by a Double Expansion technique. *Phys. Fluids A*. **1992**, *4*, 1510–1520. [[CrossRef](#)]
41. Turns, S.R. *An Introduction to Combustion*; McGraw-Hill, Inc.: New York, NY, USA, 1996.
42. Beale, J.; Reitz, R. Modeling spray atomization with the Kelvin-Helmholtz/Rayleigh-Taylor hybrid model. *At. Spray* **1999**, *9*, 623–650.
43. Gonzalez, D.M.; Lian, Z.; Reitz, R. Modeling Diesel Engine Spray Vaporization and Combustion. *SAE Trans.* **1992**, *101*, 1064–1076.
44. Naber, J.; Reitz, R. Modeling Engine Spray/Wall Impingement. *SAE Trans.* **1988**, *97*, 118–140.
45. Amsden, A.; Orourke, P.; Butler, T. *KIVA-2: A Computer Program for Chemically Reactive Flows with Sprays*; NASA STI/Recon Technical Report N; Report of Los Alamos National Laboratory: Los Alamos, NM, USA, 1989; Volume 89, p. 27975.
46. Fan, L.; Cheng, F.; Zhang, T.; Liu, G.; Yuan, J.; Mao, P. Visible-light photoredox-promoted desilylative allylation of *a*-silylamines: An efficient route to synthesis of homoallylic amines. *Tetrahedron Lett.* **2021**, *81*, 153357. [[CrossRef](#)]
47. Hiroyasu, H.; Kadota, T. Models for Combustion and Formation of Nitric Oxide and Soot in Direct Injection Diesel Engines. *SAE Trans.* **1976**, *85*, 513–526. [[CrossRef](#)]
48. Yousefi, A.; Guo, H.; Birouk, M. Effect of swirl ratio on NG/diesel dual-fuel combustion at low to high engine load conditions. *Appl. Energy* **2018**, *229*, 375–388. [[CrossRef](#)]
49. Liu, H.; Li, J.; Wang, J.; Wu, C.; Liu, B.; Dong, J.; Liu, T.; Ye, Y.; Wang, H.; Yao, M. Effects of injection strategies on low-speed marine engines using the dual fuel of high-pressure direct-injection natural gas and diesel. *Energy Sci. Eng.* **2019**, *7*, 375–388. [[CrossRef](#)]
50. Zheng, Z.; Li, C.; Liu, H.; Zhang, Y.; Zhong, X.; Yao, M. Experimental study on diesel conventional and low temperature combustion by fueling four isomers of butanol. *Fuel* **2015**, *141*, 109–119. [[CrossRef](#)]
51. Pan, M.; Huang, R.; Liao, J.; Jia, C.; Zhou, X.; Huang, H.; Huang, X. Experimental study of the spray, combustion, and emission performance of a diesel engine with high n-pentanol blending ratios. *Energy Convers. Manag.* **2019**, *194*, 1–10. [[CrossRef](#)]
52. Jin, C.; Zhang, X.; Geng, Z.; Pang, X.; Wang, X.; Ji, J.; Wang, G.; Liu, H. Effects of various co-solvents on the solubility between blends of soybean oil with either methanol or ethanol. *Fuel* **2019**, *244*, 461–471. [[CrossRef](#)]
53. Nayak, S.; Mishra, P.; Noor, M.M. Simultaneous reduction of nitric oxide and smoke opacity in TDI dual fuel engine fuelled with calophyllum-diesel blends and waste wood chip gas for modified inlet valve and injector nozzle geometry. *Energy* **2019**, *189*, 116238. [[CrossRef](#)]
54. Huang, H.; Zhu, Z.; Zhu, J.; Lv, D.; Pan, Y.; Wei, H.; Teng, W. Experimental and numerical study of pre-injection effects on diesel-*n*-butanol blends combustion. *Appl. Energy* **2019**, *249*, 377–391. [[CrossRef](#)]
55. Li, W.; Ji, J.; Huang, L.; Guo, Z. Global dynamics of a controlled discontinuous diffusive SIR epidemic system. *Appl. Math. Lett.* **2021**, *121*, 107420. [[CrossRef](#)]
56. Zuo, H.; Tan, J.; Wei, K.; Huang, Z.; Zhong, D.; Xie, F. Effects of different poses and wind speeds on wind-induced vibration characteristics of a dish solar concentrator system. *Renew. Energy* **2021**, *168*, 1308–1326. [[CrossRef](#)]
57. Zuo, H.; Liu, G.; E, J.; Zuo, W.; Wei, K.; Hu, W.; Tan, J.; Zhong, D. Catastrophic analysis on the stability of a large dish solar thermal power generation system with wind-induced vibration. *Sol. Energy* **2019**, *183*, 40–49. [[CrossRef](#)]
58. Zuo, H.; Zhang, B.; Huang, Z.; Wei, K.; Tan, J. Effect analysis on SOC values of the power lithium manganese battery during discharging process and its intelligent estimation. *Energy* **2022**, *238*, 121854. [[CrossRef](#)]
59. Ma, Y.; Liu, C.; E, J.; Mao, X.; Yu, Z. Research on modeling and parameter sensitivity of flow and heat transfer process in typical rectangular microchannels: From a data-driven perspective. *Int. J. Therm. Sci.* **2022**, *172*, 107356. [[CrossRef](#)]
60. E, J.; Cai, L.; Li, J.; Ding, J.; Chen, J.; Luo, B. Effects analysis on the catalytic combustion and heat transfer performance enhancement of a non-premixed hydrogen/air micro combustor. *Fuel* **2022**, *309*, 122125. [[CrossRef](#)]
61. Zhang, B.; Zuo, H.; Huang, Z.; Tan, J.; Zuo, Q. Endpoint forecast of different diesel-biodiesel soot filtration process in diesel particulate filters considering ash deposition. *Fuel* **2020**, *272*, 117678. [[CrossRef](#)]
62. E, J.; Zhao, M.; Zuo, Q.; Zhang, B.; Zhang, Z.; Peng, Q.; Han, D.; Zhao, X.; Deng, Y. Effects analysis on diesel soot continuous regeneration performance of a rotary microwave-assisted regeneration diesel particulate filter. *Fuel* **2020**, *260*, 116353. [[CrossRef](#)]
63. Feng, C.; Deng, Y.; Chen, L.; Han, W.; E, J.; Wei, K.; Han, D.; Zhang, B. Hydrocarbon emission control of a hydrocarbon adsorbent and converter under cold start of the gasoline engine. *Energy* **2022**, *239*, 122138. [[CrossRef](#)]
64. Chen, L.; Deng, Y.; Feng, C.; Han, W.; E, J.; Wang, C.; Han, D.; Zhang, B. Effects of zeolite molecular sieve on the hydrocarbon adsorbent performance of gasoline engine of during cold start. *Fuel* **2022**, *310*, 122427. [[CrossRef](#)]
65. E, J.; Luo, J.; Han, D.; Tan, Y.; Feng, C.; Deng, Y. Effects of different catalysts on light-off temperature of volatile organic components in the rotary diesel particulate filter during the regeneration. *Fuel* **2022**, *310*, 122451. [[CrossRef](#)]
66. Zhang, Z.; Ye, J.; Lv, J.; Xu, W.; Tan, D.; Jiang, F.; Huang, H. Investigation on the effects of non-uniform porosity catalyst on SCR characteristic based on the field synergy analysis. *J. Environ. Chem. Eng.* **2022**, *10*(2), 107056. [[CrossRef](#)]
67. E, J.; Liu, G.; Zhang, Z.; Han, D.; Chen, J.; Wei, K.; Gong, J.; Yin, Z. Effect analysis on cold starting performance enhancement of a diesel engine fueled with biodiesel fuel based on an improved thermodynamic model. *Appl. Energy* **2019**, *243*, 321–335. [[CrossRef](#)]
68. Zhang, Z.; E, J.; Deng, Y.; Pham, M.; Zuo, W.; Peng, Q.; Yin, Z. Effects of fatty acid methyl esters proportion on combustion and emission characteristics of a biodiesel fueled marine diesel engine. *Energy Convers. Manag.* **2018**, *159*, 244–253. [[CrossRef](#)]